Green Chemistry

TUTORIAL REVIEW

View Article Online
View Journal | View Issue

Cite this: *Green Chem.*, 2024, **26**, 4987

Recent progress in transition metal based catalysts and mechanism analysis for alcohol electrooxidation reactions

Yuguo Zhao,[a,b] Emma M. Björk,[b] Yong Yan,*[a] Peter Schaaf[c] and Dong Wang*[c]

In order to address energy and environmental challenges effectively, there is a need to promote renewable energy-driven electrochemical conversion technologies, particularly electrosynthesis. Electrosynthesis has the potential to convert abundant molecules into valuable chemicals and fuels. However, the widespread adoption of electrosynthesis is often hindered by the slow oxygen evolution reaction (OER). To overcome this limitation, we can employ the more efficient alcohol electrooxidation reaction (AOR), utilizing renewable biomass-derived alcohols as an alternative to OER for producing high-value chemicals. Consequently, the development of efficient AOR catalysts, in conjunction with cathodic reduction reactions (hydrogen evolution, oxygen, and nitrogen electroreduction, *etc.*), is crucial for sustainable and environmentally-friendly advancements. A thorough understanding of AOR mechanisms is essential for catalyst design and can be achieved through the utilization of *in situ* characterization techniques and density functional theory (DFT) calculations. This review summarizes recent progress in AOR catalysts, with a particular focus on the electrooxidation of monohydric alcohols, polyols, and associated studies on reaction mechanisms. Additionally, the review identifies key factors impeding AOR development and provides insights into future prospects.

Received 15th January 2024,
Accepted 25th March 2024

DOI: 10.1039/d4gc00227j

rsc.li/greenchem

1. Introduction

As the global energy and environmental crisis escalates, the advancement of electrochemical conversion technologies, powered by renewable energy sources like solar and wind, has become increasingly crucial.[1–3] Electrosynthesis is recognized as an effective strategy to mitigate this crisis, as it enables the transformation of Earth-abundant molecules into valuable chemical products and transportable fuels.[4,5] Often, this process involves coupling numerous cathodic electrochemical reduction reactions, such as the hydrogen evolution,[6,7] oxygen,[8,9] nitrogen,[10,11] or carbon dioxide electroreduction,[12,13] with the oxygen evolution reaction (OER). However, the slow kinetics and thermodynamics of OER at the anode present significant challenges for large-scale application of these processes. Furthermore, the limited value of the oxygen (O_2) product exacerbates this issue.[14] As a result, extensive research has been conducted to explore organic electrooxidation reactions (OORs) as more efficient alternatives to OER.[15,16] These reactions not only exhibit lower overpotentials compared to OER but also yield high-value products at the anode.

One prominent reaction within OORs is the alcohol electrooxidation reaction (AOR). This reaction involves the oxidation of biomass-derived alcohols, which are renewable and abundant. These alcohols are widely utilized in the manufacturing of commodity chemicals, such as formic acid, 2,5-furandicarboxylic acid, and dihydroxyacetone, among others.[17,18] However, converting biomass-derived alcohols to value-added chemical products and fuels in traditional industries often requires harsh conditions, such as high temperatures and pressures, leading to the depletion of fossil energy resources and environmental pollution.[19] Given the rising consumption of fossil energy and the negative impacts of environmental pollution, developing efficient AOR systems coupled with cathodic electroreduction is imperative for promoting sustainable global development. The success of this approach largely depends on the design and fabrication of highly efficient and

[a]*Center of Excellence for Environmental Safety and Biological Effects, Beijing Key Laboratory for Green Catalysis and Separation, Department of Chemistry, Beijing University of Technology, 100124 Beijing, China. E-mail: yong.yan@bjut.edu.cn*
[b]*Nanostructured Materials, Department of Physics, Chemistry and Biology (IFM), Linköping University, SE 58183 Linköping, Sweden*
[c]*Chair Materials for Electrical Engineering and Electronics, Institute of Materials Science and Engineering and Institute of Micro and Nanotechnologies MacroNano, TU Ilmenau, Gustav-Kirchhoff-Str. 5, 98693 Ilmenau, Germany. E-mail: dong.wang@tu-ilmenau.de*

selective catalysts for AOR. Thus, a timely and comprehensive review of this subject is vital for a deeper understanding of AOR and its potential implications.

This review aims to provide a detailed summary of recent advancements in transition metal-based catalysts. It primarily focuses on transition metals and their compounds, which have shown a high potential in the field of AOR. This potential arises from their well-regulated d orbitals and abundant presence on Earth.[20] The review specifically summarizes the electrooxidation processes of monohydric alcohols and polyols in the context of AOR. Additionally, characteristic comparisons between representative AOR and OER are provided in Table 1. The applications of the products from these reactions, along with their respective reaction pathways, are also discussed. Understanding the reaction mechanisms of AOR is crucial for designing efficient catalysts, necessitating investigations into these mechanisms through advanced *in situ* characterization techniques and density functional theory (DFT) calculations. Therefore, this review emphasizes mechanism studies utilizing *in situ* characterization and DFT calculations, aiding comprehension of the relationship between catalyst structure and catalytic performance. Finally, the review concludes with an analysis of the challenges hindering AOR development and insights into future prospects in this field, hoping to guide efficient catalyst design.

2. Alcohol electrooxidation reaction

The development of AOR systems has gained significant attention worldwide in recent years. Beyond the previously mentioned advantages, AOR also offers benefits such as safety, increased current density, and potential for fine chemical production. AOR is safer than OER in traditional water-splitting systems, as it minimizes O_2 production, reducing risks associated with O_2 and hydrogen (H_2) mixing. This aspect mitigates safety concerns and potential hazards. AOR's ability to achieve higher current densities at the same voltage conditions, due to reduced overpotential, enhances the energy utilization efficiency of the system. Additionally, AOR is highly significant in the production of fine chemicals, laying the foundation for future development of high-efficiency electrocatalytic synthesis of fine chemicals.[25–29] These advantages make AOR an attractive and promising electrochemical reaction system with the potential to contribute to clean and efficient chemical synthesis.

This section offers an overview of representative catalysts for AOR, covering both monohydric alcohols and polyols. It investigates the reaction pathways associated with these catalysts and compiles a summary of recently reported catalyst performances for AOR in Table 2.

2.1 Monohydric alcohols

2.1.1 Methanol. Methanol molecule, with its ready availability and cost-effectiveness, has attracted substantial attention in scientific research.[30] Its simple C_1-type alcohol molecular structure makes it an ideal model for studying various chemical transformations in organic synthesis. Methanol is instrumental in affecting C–H, C–O, and O–H bonds, facilitating processes like alcohol-water reforming and electrochemical C–C coupling reactions. These transformations are essential for synthesizing a broad range of valuable chemicals.[31–33] The primary products of methanol oxidation reaction (MOR), such as formic acid or formate, are extensively used in commodities and provide significant value-added benefits. Thus, electrocatalytic MOR has become a focal point of research in this area.

Among the catalysts explored for MOR, those based on earth-abundant transition metals, especially in alkaline media, have received notable attention. A study by Li *et al.* introduced the Ni_3B/Ni catalyst, termed NiB-400, synthesized by reacting sodium borohydride ($NaBH_4$) with nickel nitrate, followed by annealing.[14] NiB-400's crystal structure, shown in Fig. 1a, features numerous interfaces. Regarding MOR performance, NiB-400 demonstrated efficient catalytic activity in 1 M KOH electrolyte, achieving a current density of 175 mA cm^{-2} at a relatively low overpotential of 1.61 V *vs.* RHE (Fig. 1b). Additionally, the catalyst exhibited nearly 100% faradaic efficiency (FE) over a broad potential range (1.41–1.71 V *vs.* RHE), as depicted in Fig. 1c. To better understand NiB-400's efficient MOR performance, additional DFT calculations was conducted. The potential-determining steps for MOR was identified as the $*CH_3O \rightarrow *CH_2O + H^+ + e^-$ reaction on Ni,

Table 1 The comparison between representative AOR systems and OER

Reactions	Theoretical oxidation potential	Disadvantages/Challenges
Water → Oxygen $4\ OH^- \rightarrow 2\ H_2O + O_2 + 4\ e^-$	1.23 V (ref. 21)	Low energy conversion efficiency O_2 is less valuable
Methanol → HCOOH $CH_3OH + 4\ OH^- \rightarrow HCOOH + 3\ H_2O + 4\ e^-$	0.103 V (ref. 21)	HCOOH is easily overoxidized to CO_2
Benzyl alcohol → Benzoic acid $Ph\text{-}CH_2OH + 4\ OH^- \rightarrow Ph\text{-}COOH + 3\ H_2O + 4\ e^-$	0.48 V (ref. 22)	The product separation process is complex
HMF → FDCA $HMF + 6\ OH^- \rightarrow FDCA + 4\ H_2O + 6\ e^-$	0.30 V (ref. 23)	HMF is unstable in the electrolyte
Glycerol → HCOOH $C_3H_8O_3 + 8\ OH^- \rightarrow 3\ HCOOH + 5H_2O + 8\ e^-$	0.69 V (ref. 24)	The selectivity of aldehydes or ketones is low

HMF: 5-hydroxymethylfurfural; FDCA: 2,5-furandicarboxylic acid.

Table 2 The recently reported catalyst performances of AOR

Catalyst	Electrolyte	Main product	J (mA cm^{-2})/E (V *vs.* RHE)	Conversion (%)	FE (%)	Ref.
Fe-NF-500	1 M KOH/1 M methanol	Formate	10/1.328	NA	>98	34
h-NiSe/CNTs	1 M KOH/1 M methanol	Formate	10/1.37	NA	>95	33
NiB-400	1 M KOH/1 M methanol	Formate	10/1.465	NA	~100	14
Ni_3C particles/C	1 M KOH/1 M methanol	Formate	10/1.43	~100	NA	48
$Ni_{0.75}Fe_{0.25}Se_2$	1 M KOH/1 M methanol	Formate	53.5/1.5	NA	99	49
β-$Co_{0.1}Ni_{0.9}(OH)_2$/NF	1 M KOH/0.05 M ethanol	Acetate	100/1.35	100	95	50
CoNi-PHNs	1 M KOH/1 M ethanol	Acetate	57/1.5	NA	99	51
Ni_3S_2 NWs/C	1 M KOH/1 M ethanol	Acetate	107/1.5	NA	NA	52
NiO_x/CN_x	1 M KOH/1 M ethanol	Acetate	10/1.354	NA	NA	53
Cu-doped NiOOH	1 M KOH/1 M ethanol	Acetate	227/1.72	NA	>98	54
$Ni_{0.75}Co_{0.25}Se_2$ NPs	1 M KOH/1 M ethanol	Acetate	81.6/1.55	NA	82.2	55
A–Ni–Co–H/NF	1 M KOH/0.1 M BA	BAc	100/1.35	99.6	93.5	22
N–Mo–Ni/NF	1 M KOH/0.1 M BA	BAc	100/1.338	99.1	98.7	56
h-$Ni(OH)_2$	1 M KOH/0.04 M BA	BAc	40/>1.4	99.99	98.62	57
NiO/Ni_3S_2	1 M KOH/0.2 M BA	BAc	50/1.391	99.11	94	58
Ni–OH/NF	1 M KOH/0.1 M BA	BAc	100/1.33	84.5	99	59
hp-Ni	1 M KOH/0.01 M BA	BAc	10/1.35	NA	98	60
NiB_x–P_y	1 M KOH/0.01 M HMF	FDCA	NA	99	92.5	61
NiCoP	1 M KOH/0.3 M HMF	FDCA	10/1.26	98.7	95.8	62
NiFe LDH	1 M KOH/0.01 M HMF	FDCA	10/1.32	99	99.4	63
NiS_x/Ni_2P	1 M KOH/0.01 M HMF	FDCA	10/1.34	100	95.1	64
NiB_x	1 M KOH/0.01 M HMF	FDCA	10/1.33	99.8	99.5	65
NiSe@NiO_x	1 M KOH/0.01 M HMF	FDCA	50/1.35	100	99	66
$NiCo_2O_4$	1 M KOH/0.005 M HMF	FDCA	10/1.47	99.6	87.5	67
MoO_2–FeP@C	1 M KOH/0.01 M HMF	FDCA	10/1.359	99.4	97.8	68
Ru_1–NiO	1 M PBS/0.05 M HMF	DFF	10/1.283	72.4	43.3	69
Rh–SA/NiFe NMLDH	1 M PBS/0.05 M HMF	FDCA	50/1.27	98	98.5	70
Ni-VN/NF	1 M KOH/0.01 M HMF	FDCA	10/1.352	>99	98.8	71
CoNiP-NIE	1 M KOH/0.01 M HMF	FDCA	20/1.29	NA	87.2	72
$CoNi_{0.25}P$	1 M KOH/0.3 M EG	Formate	10/1.24	100	82.5	73
Pd–$Ni(OH)_2$/NF	1 M KOH/1 M EG	GA	100/0.69	93.2	86	74
Branched $NiSe_2$/C	1 M KOH/1 M EG	Formate	103.6/1.6	NA	~80	75
Ni–Mo–N/NC	1 M KOH/0.1 M glycerol	Formate	50/1.25	86	96.7	76
E-NiV LDH	1 M KOH/0.1 M glycerol	Formate	10/1.23	98	94	77
$CoMoO_4$	1 M KOH/0.1 M Glycerol	Formate	10/1.239	NA	90	78
Bi–Co_3O_4	1 M KOH/0.1 M glycerol	Formate	10/1.223	NA	97.05 ± 2.55	79
Mn–$CoSe_2$/CFC	1 M KOH/0.1 M glycerol	Formate	10/1.27	NA	~95	80
Ni–Mo–N/CFC	1 M KOH/0.1 M glycerol	Formate	10/1.3	NA	~97	24
MnO_2	0.005 M H_2SO_4/0.2 M glycerol	Formic acid	10/1.36	NA	53	81
NiVRu-LDHs NAs/NF	1 M KOH/0.1 M glycerol	Formate	10/1.24	NA	97	82
$NiFeO_x$–NF	1 M KOH/0.5 M glucose	Glucaric acid	NA	98.3	87	83
Co@NPC800	1 M KOH/0.1 M glucose	Lactate	10/1.46	NA	NA	84
$Cu(OH)_2$	1 M KOH/0.1 M glucose	Gluconic acid	NA	NA	98.7	85

BAc: benzoic acid; HMF: 5-hydroxymethylfurfural; FDCA: 2,5-furandicarboxylic acid; DFF: 2,5-diformylfuran; EG: ethylene glycol; GA: glycolic acid; NA: not available.

Ni_3B, and Ni_3B/Ni surfaces. Notably, the Ni_3B(001)/Ni(111) heterostructure displayed the lowest Gibbs energy barrier for MOR, suggesting optimal activity on this surface. Additionally, the partial density of states (PDOS) was calculated to analyze the adsorption behavior of the *CH_2O intermediate on the Ni_3B(001)/Ni(111) heterostructure, as well as on Ni_3B and Ni structures. Fig. 1e illustrates the d-band center values of Ni_3B/Ni heterostructure, Ni_3B, and Ni as −1.22, −1.26, and −1.34 eV, respectively. Importantly, the d-band center of the Ni_3B/Ni heterostructure is closest to the Fermi energy level, indicating its superior adsorption capacity for *CH_2O. This effectively promotes the binding of the key intermediate and reduces the associated energy barrier, thus, enhancing catalytic activity. The synthesis of NiB-400 and subsequent DFT studies offer profound insights into the exceptional MOR performance of the nickel Ni_3B/Ni catalyst.

Similar enhancements in MOR performance have been observed in various catalysts with heterostructure configurations, including Fe_2O_3/NiO,[34] NMS/CC,[35] h-NiSe/CNTs,[33] $FeNi_2S_4$/NiS-NG-2,[36] NiFe-LDH/NiFe-HAB,[37] NiCoP/MoS_2,[38] and 3D Ni/NiO/RG-400.[39] These studies show that the heterogeneous structure of these catalysts significantly improves their electronic configuration, enhancing adsorption capacity for key intermediates and reducing associated energy barriers.

Core–shell catalysts like CuS@CuO/CF,[40] Cu/NiCu NWs-220,[41] Au@PdRu RNs,[42] and Mo_2C/MWCNT[43] have also exhibited effcient MOR performance. They modulate electronic structure through lattice strain modification at the heterointerface,

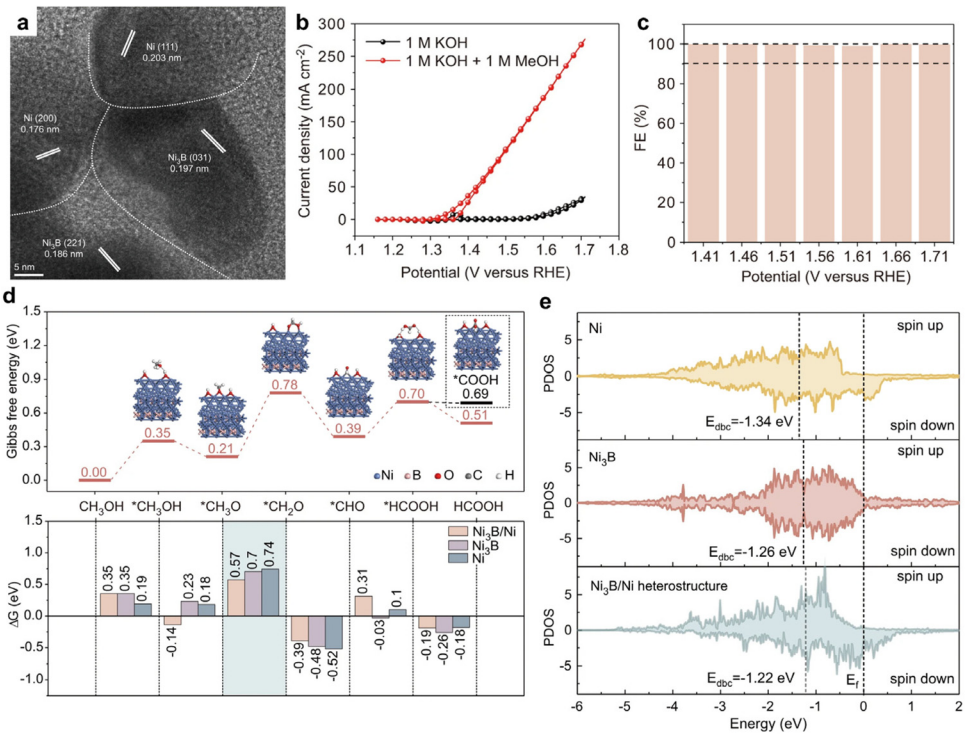

Fig. 1 (a) TEM image of NiB-400. (b) CV curves of NiB-400 for MOR and OER. (c) The faradaic efficiency of formate was obtained by MOR at different potentials for 1 h. (d) Gibbs free energy diagram of MOR occurring on $Ni_3B(001)/Ni(111)$ heterostructure. (e) Partial density of states (PDOS) of Ni active sites for different structures. Reproduced with permission from ref. 14. Copyright 2022 Springer Nature.

influencing interaction with intermediates as explained by d-band theory.[44,45] This tunability of electronic structure in core–shell catalysts represents a promising direction for optimizing the catalytic activity in MOR.

2.1.2 Benzyl alcohol. There are two primary pathways for the oxidation reaction of benzyl alcohol. The first pathway involves a two-electron process, resulting in the creation of benzaldehyde, while the second pathway entails a four-electron process leading to the generation of benzoic acid (Fig. 2). The resultant product of oxidation, benzaldehyde, assumes a crucial role as an intermediate in the production of fine chemicals, fragrances, and flavor additives. In contrast, benzoic acid, also produced during oxidation, finds diverse applications in the pharmaceutical, chemical, and food industries.[46,47] Hence, the oxidation of benzyl alcohol holds substantial industrial significance as an alcohol oxidation reaction. Regrettably, present industrial oxidation methods heavily depend on energy consumption and may pose environmental hazards due to pollution. Electrooxidation presents a promising alternative solution to address these challenges.

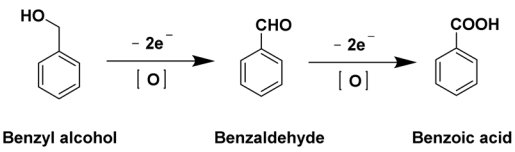

Fig. 2 The reaction pathways for the oxidation of benzyl alcohol.

Recent studies have focused on developing well-designed catalysts for benzyl alcohol oxidation reaction (BOR). Wang *et al.*[86] introduced a self-supported layered porous $NC@CuCo_2N_x/CF$ catalyst, as depicted in Fig. 3a–d. This catalyst demonstrated high efficiency as a bifunctional catalyst for BOR and hydrogen evolution in alkaline electrolyte solutions (pH 14). Fig. 3e shows that, without benzyl alcohol, over 1.46 V *vs.* RHE was needed to achieve a current density of 10 mA cm^{-2}. However, this requirement dropped to 1.25 V *vs.* RHE with the addition of benzyl alcohol, indicating a preference for BOR over oxygen evolution. In a bifunctional electrolytic system (HER and BOR), $NC@CuCo_2N_x/CF$ showed excellent

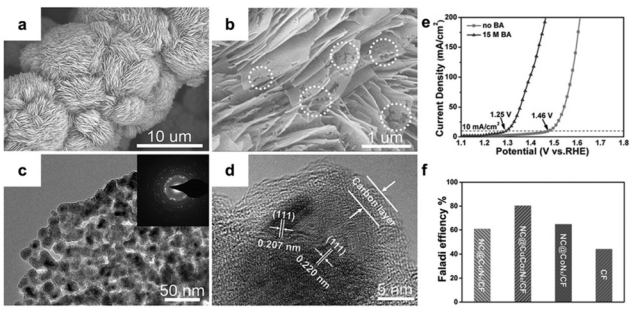

Fig. 3 (a–d) Structural characterization of $NC@CuCo_2N_x/CF$. (e) LSV curves of OER and BOR. (f) faradaic efficiency of BOR using different catalysts. Reproduced with permission from ref. 86. Copyright 2017 Wiley-VCH.

BOR performance with higher FE compared to other catalysts (Fig. 3f). The good performance of NC@$CuCo_2N_x$/CF is attributed to its unique layered porous structure, which enhances surface area and ion diffusion. Additionally, the cooperative effect of Cu_3N and $Co_{5.47}N$ optimizes the adsorption energy of key intermediates, improving reaction kinetics and electrocatalytic activity.

Qiu *et al.*[22] used a hydrothermal synthesis method to create Ni and Co hydroxide nanosheets on a Ni foam substrate (A–Ni–Co–H/NF), shown in Fig. 4a and b. This material offers a large active surface area and lower charge transfer resistance. Without benzyl alcohol, achieving an OER current density of 100 mA cm^{-2} required a voltage of 1.60 V. This decreased to 1.35 V with the addition of benzyl alcohol, enabling the attainment of an industrial-scale current density above 400 mA cm^{-2} for electrocatalytic oxidation of benzyl alcohol without undergoing OER. In contrast, the NF substrate could not reach 100 mA cm^{-2} even with benzyl alcohol (BA) (Fig. 4c). The stability of the catalyst was investigated through five repeated amperometric tests at a consistent potential of 1.5 V. As depicted in Fig. 4e and f, the conversion of BA remained consistently above 99%, with the yield of Ph-COOH maintaining a level of over 95% throughout the five trials. Additionally, the FE for Ph-COOH production was consistently maintained at 90–95%.

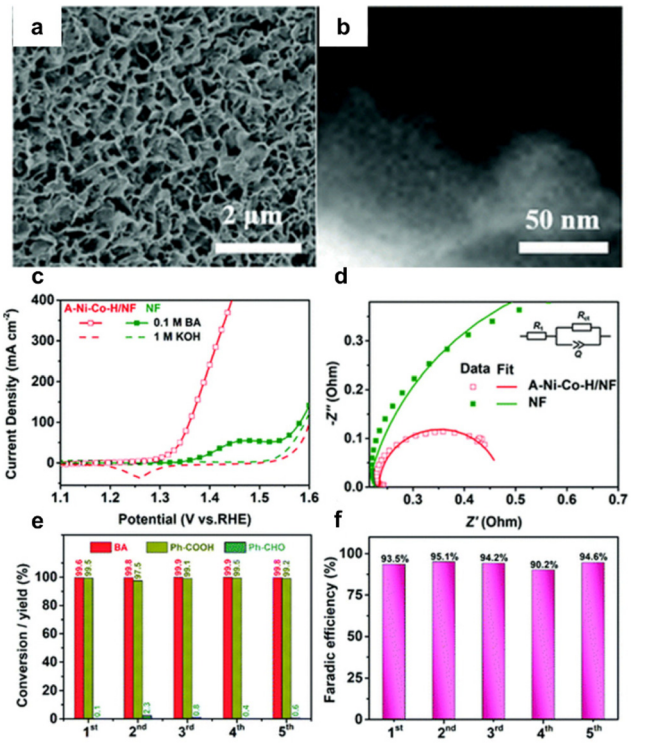

Fig. 4 (a and b) Structural characterization of A–Ni–Co–H/NF, (c) LSV curves of A–Ni–Co–H/NF and NF in 1 M KOH electrolyte with and without 0.1 M benzyl alcohol, (d) electrochemical impedance spectroscopies of A–Ni–Co–H/NF and NF, (e) conversion and yield of Ph-COOH after five successive electrolysis cycles, and (f) faradaic efficiency of Ph-COOH corresponding to panel (e). Reproduced with permission from ref. 22. Copyright 2020 Royal Society of Chemistry.

2.1.3 5-hydroxymethylfurfural. 5-Hydroxymethylfurfural (HMF) is an important biomass-derived compound, typically produced through the dehydration of carbohydrates like sugars, glucose, cellulose, inulin, starch, and cellulose.[87–89] The HMF oxidation reaction (HMFOR) leads to the formation of valuable products such as 2,5-diformylfuran (DFF), 5-(hydroxymethyl)furfural carboxylic acid (HMFCA), and 2,5-furandicarboxylic acid (FDCA), as depicted in Fig. 5. These compounds are extensively used as precursors or intermediates in the polymer industry, chemical manufacturing, and pharmaceuticals. Their production predominantly involves the selective oxidation of aldehydes or hydroxymethyl groups.[90–93] Among these, FDCA is particularly valuable and serves as an eco-friendly alternative to petroleum-based terephthalic acid.[62,94,95] The U.S. Department of Energy has listed FDCA as one of the top 12 sugar-derived platform chemicals.[96,97] Traditionally, FDCA production from HMF has involved oxidation under alkaline conditions, requiring high temperatures and pressures, and the use of precious metal catalysts such as Au, Pt, and Pd.[98,99] However, this process poses sustainability challenges. Consequently, there has been growing interest in developing electrocatalytic oxidation technologies that offer milder reaction conditions and are more environmentally friendly for producing FDCA.

Nickel-based materials have garnered significant interest as electrocatalysts for HMFOR, owing to their high activity and cost-effectiveness.[100] In a study by Sun *et al.*,[101] a bimetallic Ni–Cu catalyst supported on Ni foam (Ni–Cu/NF) was developed for efficient HMFOR. Structural analysis indicated a non-uniform distribution of the Ni–Cu catalyst on the Ni foam surface. Additionally, the catalyst was in an amorphous state, with Ni, Cu, and O elements evenly dispersed, as shown in Fig. 6a–d. The Ni–Cu/NF catalyst exhibited efficient performance, with a low onset potential for HMFOR (approximately 1.35 V *vs.* RHE) and a high current density of 1000 mA cm^{-2} at 1.50 V. Notably, the potential required to achieve current densities of 200, 500, and 1000 mA cm^{-2} was over 200 mV lower than that for the oxygen evolution reaction (OER), as demonstrated in Fig. 6e and f. The Ni–Cu/NF catalyst also showed remarkable stability over 70 consecutive cycles, maintaining consistent performance without significant degradation, as depicted in Fig. 6g. During the stability evaluation, FEs and yields of FDCA remained above 95%, indicating the efficient

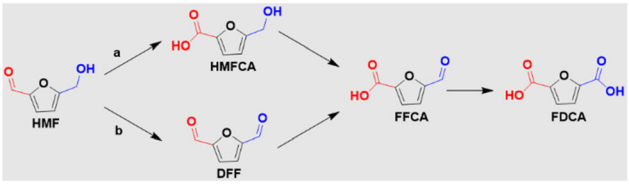

Fig. 5 The HMF electrooxidation reaction pathway.

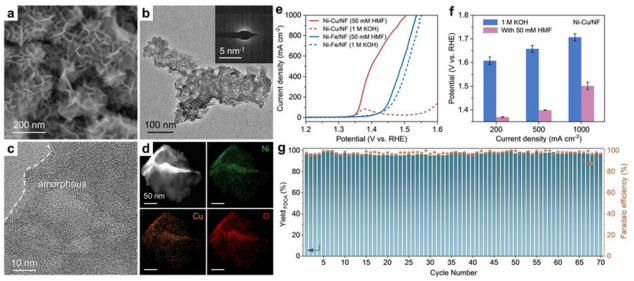

Fig. 6 (a–d) Structural characterization of Ni-Cu/NF. (e) LSV curves of Ni–Cu/NF and Ni–Fe/NF (reference sample) compared with and without the presence of 50 mM HMF in a 1 M KOH solution, with 100% iR compensation. (f) Potential required by Ni–Cu/NF to achieve different current densities in the presence or absence of 50 mM HMF. (g) Stability, yield, and faradaic efficiency of FDCA for Ni–Cu/NF with the addition of 50 mM HMF over 70 consecutive cycles at 1.45 V *vs.* RHE, with each cycle lasting for 60 min. Reproduced with permission from ref. 101. Copyright 2023 Wiley-VCH.

utility of the catalyst for biomass upgrading and its substantial practical application value.

Wang *et al.*[102] explored an electrocatalyst known as $Mn_{0.2}NiS$/GF, demonstrating promising HMFOR to FDCA conversion. This electrocatalyst showed an industrial-level current density (500 mA cm^{-2}), high FE (94.2%), and robust stability. Furthermore, other notable Ni-based electrocatalysts such as $Co_{0.4}NiS$@NF,[103] NiS_x/β-$Ni(OH)_2$/Ni,[104] Co_9S_8@Ni_3S_2/NF,[105] and NiMoO-Ni[106] also exhibited high FDCA conversion rates. These findings underscore the significant potential of Ni-based electrocatalysts in HMFOR-to-FDCA conversion and offer valuable insights for developing highly efficient electrocatalysts.

2,5-Bis(hydroxymethyl)furan (BHMF) has a structural similarity to HMF and can be obtained by the selective hydrogenation of HMF.[107] It can be further oxidized to FDCA through electrocatalysis (Fig. 7), which has recently attracted significant attention due to its higher stability in electrolytes compared to HMF.[108] A study by Chen *et al.*[109] introduced a NiCo/CF electrocatalyst for the efficient electrooxidation of BHMF, demonstrating a substantial current density of 1981.7 mA cm^{-2} at 2.293 V *vs.* RHE. This electrocatalyst also exhibited high yields and faradaic efficiencies of FDCA production, reaching 95.4% and 96.5% respectively, at a relatively low potential of 1.4 V *vs.* RHE. Moreover, Zhang *et al.*[108] reported the use of CoOOH/Ni electrodes for the effective electrooxidation of BHMF, achieving complete conversion and a high FDCA yield of 90.2%. These findings suggest that BHMF is a promising candidate for the production of FDCA through mild electrocatalysis.

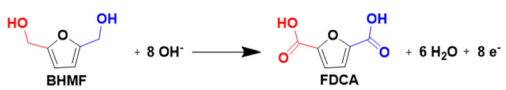

Fig. 7 The BHMF electrooxidation reaction pathway.

2.2 Polyols

2.2.1 Glycerol. Glycerol, also known as glycerin, is a versatile trihydroxy chemical intermediate predominantly generated as a byproduct in biodiesel production, as depicted in Fig. 8. Although applicable in pharmaceuticals, cosmetics, food additives, coatings, polyols, glycerides, tobacco, explosives, and other products, the market demand for glycerol is considerably lower than its production, particularly with the rapid growth of the biodiesel industry. Converting glycerol into high-value-added chemical products is an effective strategy to mitigate glycerol surplus (their application as outlined in Table 3). Traditional conversion methods in industries typically involve high energy consumption, elevated temperatures, high pressure, and O_2 introduction, posing environmental risks. Thus, the adoption of green and efficient methods for glycerol conversion into high-value-added products is crucial.

Compared to traditional industrial production, using electrocatalytic oxidation involves milder reaction conditions and effectively resolves the issues that may arise in traditional industrial glycerol oxidation, and the reaction pathways of glycerol electrooxidation as shown in Fig. 9. Recent research efforts have been centered on the development of highly efficient and cost-effective electrocatalysts for glycerol oxidation reaction (GOR). A notable advancement in this area is the use of bimetallic electrocatalysts, exemplified by $NiCo_2O_4$/NF, investigated by Shi *et al.*[110] This electrocatalyst, syn-

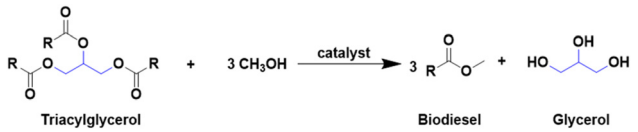

Fig. 8 Schematic illustration of glycerol production from biomass.

Table 3 Main products of GOR and their application

Product	Application
Dihydroxyacetone	Used in cosmetic and food industries,[111] pharmaceutical intermediate,[112] synthon in organic chemistry,[113] monomer in polymeric biomaterials[114]
Glyceric acid	Used in medicine: as a metabolite in the glycolysis cycle, as an intermediate in the synthesis of aminoacids,[115] acting as base materials for functional surfactants and monomers for oligoesters or polymers,[116] used for treatment of skin diseases[114]
Tartronic acid	Used as a pharmaceutical for weight loss and prevention of coronary heart disease,[117] used as a pharmaceutical and anti-corrosive protective agent, as well as for the monomer of biopolymers[118]
Mesoxalic acid	Organic synthon,[113] anti-HIV agent,[119] salt form isused in the treatment of diabetes[119]
Glycolic acid	Degreasing and rust removal,[120] as a major raw material in the fields of fine chemistry and pharmacy[121]
Formic acid	Chemical raw material widely used in the tanning, pharmaceutical, pesticide,[122] fuel in fuel cell[123]

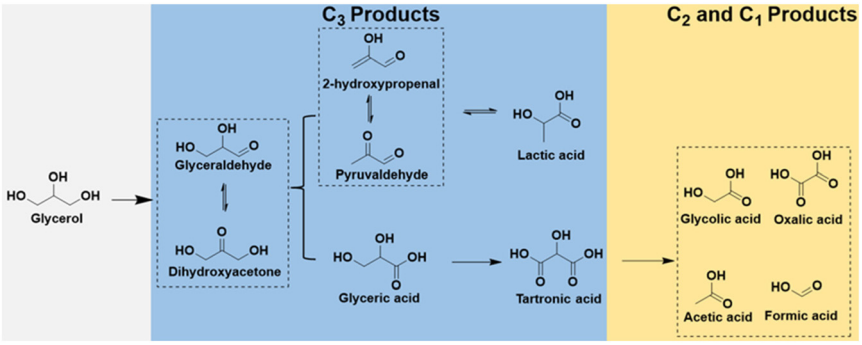

Fig. 9 Schematic illustration of electrooxidation pathway of glycerol.

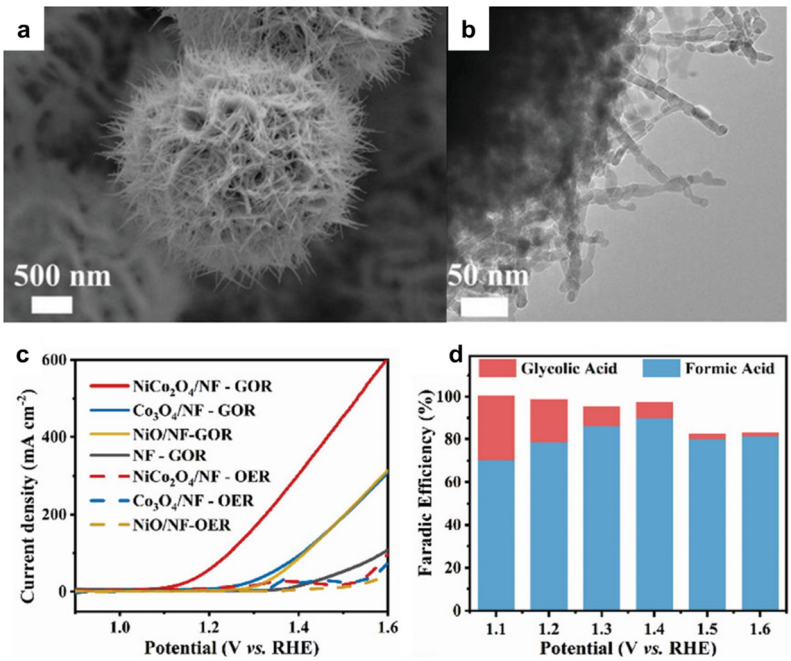

Fig. 10 (a) SEM (b) TEM images of $NiCo_2O_4$/NF. (c) LSV curves of $NiCo_2O_4$/NF and other reference samples in 1 M KOH with and without 0.1 M glycerol. (d) faradaic efficiency of products obtained by conducting CA tests at different potentials. Reproduced with permission from ref. 110. Copyright 2023 Wiley-VCH.

thesized through hydrothermal and calcination processes, featured a distinctive 3D nanoneedle array structure, as shown in Fig. 10a and b. In GOR, $NiCo_2O_4$/NF, along with other tested samples, demonstrated significantly lower onset potential and higher current density than those in the OER. Specifically, $NiCo_2O_4$/NF's onset potential for GOR was about 400 mV lower than that of OER, underlining its superior performance in GOR applications. Chronoamperometry (CA) tests at various potentials showed that the formic acid production's FE peaked at 89.9% at 1.40 V *vs.* RHE. This result underscores $NiCo_2O_4$/NF's efficacy as an electrocatalyst for GOR, suggesting its potential in advancing the development of more effective and economical catalysts for these processes.

2.2.2 Glucose. Glucose, a commonly sourced biomass feedstock produced through cellulose hydrolysis (Fig. 11).[124] It

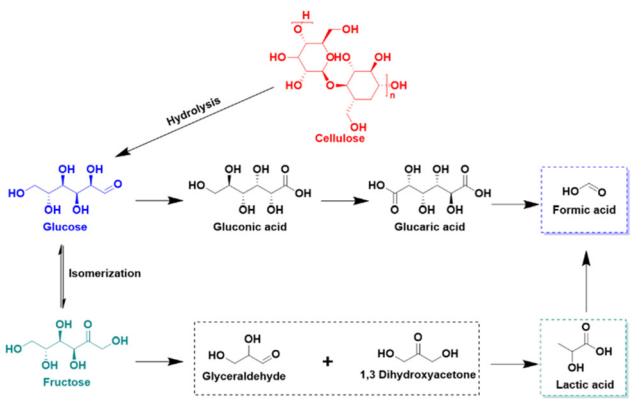

Fig. 11 Glucose production from biomass hydrolysis and electrooxidation pathway of glucose.

serves as a precursor for various high-value chemicals such as gluconic acid, glucaric acid, lactic acid, and formic acid, finding applications in food, pharmaceutical, and chemical industries.[125,126] However, traditional industrial methods for these chemicals are complex and unsustainable. For example, lactic acid production often involves glucose fermentation, generating substantial wastewater,[127] and glucaric acid production typically requires chemical oxidation with nitric acid, posing environmental concerns.[128] To address these challenges, electrooxidation of glucose has emerged as a sustainable and efficient alternative, with reaction pathways detailed in Fig. 11.

For glucose electrooxidation, Duan *et al.*[129] reported an efficient electrocatalyst, CoOOH/CC, synthesized using an electrochemical method. SEM and HAADF–STEM analyses confirmed its interconnected array structure (Fig. 12a and b). Fig. 12c showed that, with the addition of 0.1 M glucose, the onset potential for glucose oxidation was 200 mV lower than that for OER. This indicates easier glucose oxidation with more favorable dynamics and thermodynamics compared to water oxidation. CoOOH/CC displayed significant performance in converting glucose to formate across a broad potential window of 1.3–1.7 V *vs.* RHE, achieving 60–70% FE, as demonstrated in Fig. 12d (reactions were conducted in a custom/upgraded reactor).

Additional research has identified several other electrocatalysts for glucose oxidation. For instance, CuO/CF[130] exhibited a high FE of 95.34% ± 2.20% for formate production at 1.4 V *vs.* RHE in an alkaline solution. Moreover, other electrocatalysts have shown capabilities in producing various high-value chemicals. For example, $Fe_{0.1}$–CoS_2[131] reached a low onset potential of 1.22 V *vs.* RHE for 10 mA cm^{-2} and achieved an 86.7% FE for gluconate production, while oxidized Cu[132] resulted in a 23.3% yield for lactate production, both conducted in alkaline solutions.

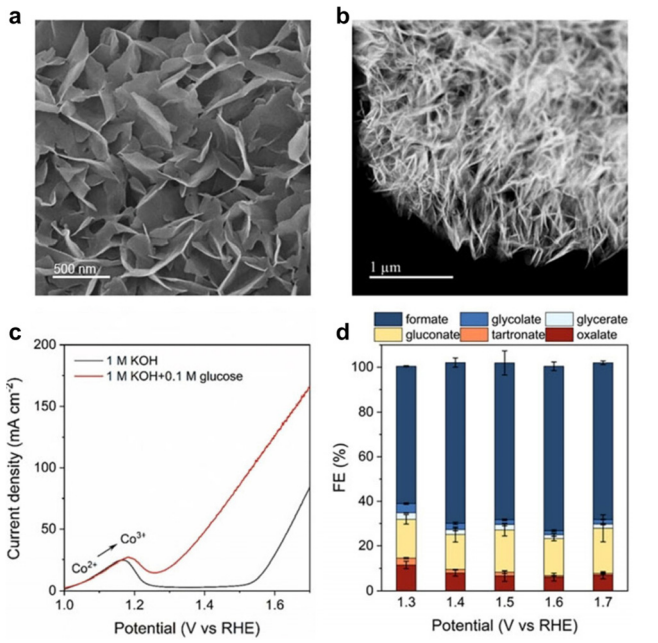

Fig. 12 (a) SEM (b) HAADF–STEM images of CoOOH/CC. (c) LSV curves of CoOOH/CC in 1 M KOH with 0.1 M glucose and without 0.1 M glucose. (d) faradaic efficiency of products at different applied potentials. Reproduced with permission from ref. 129. Copyright 2023 Wiley-VCH.

2.3 Selectivity and stability of AOR's catalyst

The above analysis primarily focuses on catalyst activity. However, selectivity and stability are also two critical factors for catalyst design. Achieving incomplete oxidation products, such as aldehydes and ketones, is of utmost importance due to their higher value compared to fully oxidized products like acids. Fine-tuning the catalyst selectivity remains a challenge, but valuable insights have already been gained. For instance, in a study by Bitter *et al.*,[133] they controlled the selectivity of glucose electrooxidation by manipulating the Pt oxidation state. They found that Pt^0 promoted glucose dialdehyde formation, exhibiting higher activity for primary alcohol dehydrogenation compared to aldehyde oxidation. In contrast, PtO_x accelerated gluconate formation, enhancing the selectivity of electrocatalytic dehydrogenation/oxidation at the anomeric carbon, albeit at the cost of primary alcohol dehydrogenation. Furthermore, the selectivity of AOR can also be adjusted through heteroatom doping. Song *et al.*[134] reported an electrocatalyst, Au_{1+n}-NiAl-LDH, which consists of both Au single atoms and Au nanoparticles on NiAl-LDH, achieving a high selectivity for the electrooxidation of benzyl alcohol to benzaldehyde (BAD). While pure NiAl-LDH displayed approximately 56% selectivity in the production of BAD, Au_{1+n}-NiAl-LDH exhibited a significantly higher selectivity of 91%. This demonstrates that the selectivity of AOR can be effectively modified through heteroatom doping. Another method to adjust selectivity is by transitioning from acids to aldehydes through the addition of 2,2,6,6-tetramethylpiperidine-*N*-oxyl (TEMPO) into the electrolyte. For instance, research by Wang *et al.*[57] showcased an electrocatalyst (1.0 h-$Ni(OH)_2$) with a selectivity of 92% for benzoic acid without the use of TEMPO. Upon the addition of TEMPO, the selectivity shifted to >94% for benzaldehyde. These findings provide valuable insights into adjusting selectivity in AOR processes.

Regarding catalyst stability, Shi's group[81] reported a catalyst (MnO_2/CP) for acidic glycerol electrooxidation with a demonstrated stabilization of over 865 hours. Mechanistic investigations revealed that long-term stability can be attributed to stabilizing the manganese oxidation state and reduced excessive oxygen vacancies, accomplished through protective interactions with glycerol. Furthermore, Duan *et al.*[135] reported that a cooperative catalyst (Au/CoOOH) exhibited significantly higher stability for the BOR compared to pure Au. By employing an intermittent potential (IP) strategy, the current density could be maintained at elevated levels (250–400 mA cm^{-2}) over a 24-hour period. The improved stability of Au/CoOOH over Au was attributed to the stronger adsorption of BA at the Au/CoOOH interface through the σ–π interaction between benzyl alkoxide and Au. Despite the potential risk of deactivation over

prolonged reactions due to the formation of AuO_x, the IP strategy effectively reduced AuO_x back to Au, thereby enhancing the overall stability of Au/CoOOH.

3. Mechanism analysis for AOR

A comprehensive understanding of the mechanisms underlying AOR systems is vital for designing and synthesizing efficient catalysts. The advancement of *in situ* technologies such as infrared (IR) spectroscopy, Raman spectroscopy, and X-ray absorption spectrum (XAS) has facilitated the tracking of active sites and reaction intermediates during AOR. These technologies enable a more detailed understanding of reaction pathways and aid in a thorough analysis of the reaction mechanism. Concurrently, DFT calculations are instrumental in elucidating the AOR mechanism, offering guidelines for electrocatalyst design. DFT calculations allow for the exploration of reaction energetics and thermodynamics, electronic structure, and reactivity of active sites, aiding in predicting and optimizing catalyst materials and properties. The integration of *in situ* technologies and DFT calculations significantly enhances the understanding of the AOR mechanism, guiding the development of more efficient electrocatalysts. This synergistic approach not only provides deep insights into reaction pathways and intermediates but also informs the design of catalysts with improved performance.

3.1 *In situ* characterization

3.1.1 *In situ* infrared spectroscopy. The fundamental principle of infrared (IR) spectroscopy is based on the selective absorption of specific infrared radiation wavelengths by molecules. This absorption correlates with the vibrational or rotational frequencies of molecular functional groups, leading to transitions between different vibrational and rotational energy levels.[136] IR spectroscopy is instrumental in analyzing characteristic vibrations and rotations of bonds in fragmented molecules, functional groups, and free radicals.[137] In electrochemical reactions, *in situ* IR spectroscopy serves as a powerful tool for real-time monitoring of the catalytic reactions, offering high sensitivity by detecting changes in dipole moments within the IR range. The technique provides critical insights into the chemical properties of adsorbates, solution species, and intermediate and product species, thus enhancing understanding of electrocatalytic mechanisms.[136,138]

There are four main working modes of *in situ* IR spectroscopy for electrocatalytic reactions: infrared reflection absorption spectroscopy (IRAS), attenuated total reflection (ATR), transmission (TIR), and diffuse reflectance Fourier transform IR (DRFTIR).[139,140] IRAS and ATR are particularly prevalent due to their shorter IR path and reduced susceptibility to external interferences. For example, Wang *et al.*[141] employed *in situ* ATR-IR spectroscopy to explore the mechanism of the MOR on NiP_x-R surfaces. The intensity of the adsorbed peak at 2920 cm^{-1}, indicative of CH_3O^* species formation, slightly increased from potentials of 1.35 V to 1.65 V (Fig. 13a). *In situ* IRAS spectra (Fig. 13b) revealed two broad bands at 1700 to 1200 cm^{-1} becoming more pronounced with increasing potential. These findings led to a proposed MOR mechanism on NiP_x-R (Fig. 13c), involving the initial adsorption of OH* and CH_3OH molecules, their subsequent reaction, and the final oxidation of CH_3O^* to produce formate (alkaline medium).

In another study by Shi *et al.*,[142] *in situ* ATR-IR spectroscopy was utilized to investigate the GOR pathways on $CuCoN_{0.6}$/CP. ATR-FTIR spectra at different potentials (ranging from 0.924 to

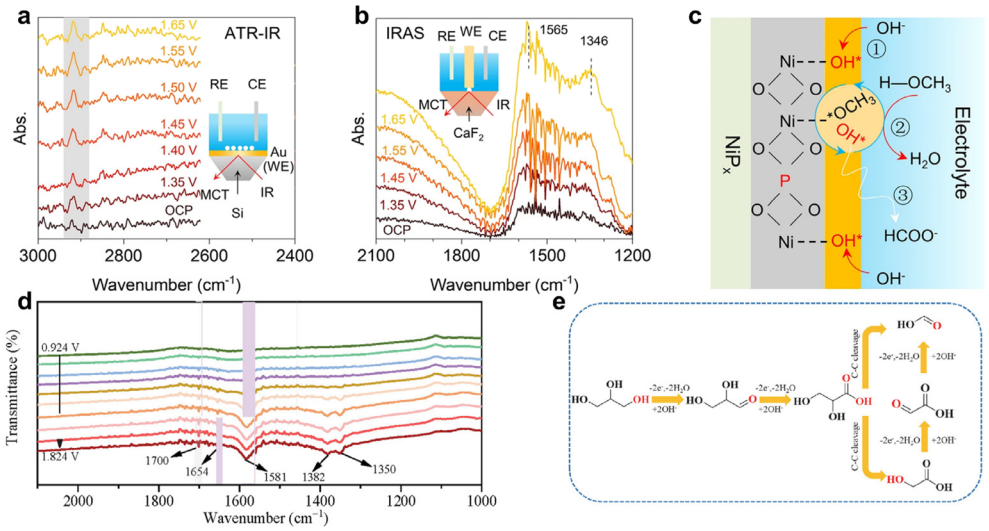

Fig. 13 (a and b) *In situ* ATR-IR and IRAS spectra on the NiP_x-R surface for the MOR process at various potentials. (c) Schematic illustration of the MOR mechanism on the NiP_x-R surface. (a–c) Reproduced with permission from ref.[141] Copyright 2022 Springer Nature. (d) *In situ* ATR-FTIR spectra for GOR on the $CuCoN_{0.6}$/CP surface. (e) Proposed reaction pathway for producing formate from GOR on $CuCoN_{0.6}$/CP in an alkaline medium. (d and e) Reproduced with permission from ref. 142. Copyright 2023 ELSEVIER.

1.824 V) were obtained to monitor reaction intermediates (Fig. 13d). Key observations included a downward peak at 1700 cm^{-1}, signifying the formation of carbonyl group-containing species like aldehydes and carboxylic acids, indicative of initial glycerol oxidation. The persistent peak at 1654 cm^{-1} across all potentials, attributed to OH bending vibration from the electrolyte, suggested glycerate formation. Additionally, the intensifying bands at 1382 and 1581 cm^{-1} with increasing potential indicated further conversion of glycerol to carboxylic acids. These ATR-IR findings, combined with NMR results, led to the proposed GOR pathway on $CuCoN_{0.6}$/CP (Fig. 13e). This pathway starts with glycerol converting to glyceraldehyde, then glyceric acid, followed by the oxidation of glyceric acid (first C–C cleavage) to form formate and glycolic acid. Through the second C–C cleavage, glycolic acid yields two formate molecules, allowing one glycerol molecule to produce up to three formate molecules, thereby maximizing carbon atom utilization.

3.1.2 ***In situ* Raman spectroscopy.** Raman spectroscopy, a robust tool for identifying molecular fingerprint information, is extensively employed in *in situ* surface analysis.[143] Compared to IR spectroscopy, Raman is less susceptible to interference from aqueous solutions and covers a broader wavenumber region, allowing for the detection of oxygen species, hydroxy, and metal-related bands. It is particularly effective in identifying metal oxide and metal hydroxide bands, often regarded as active sites for AOR. Hu *et al.*[96] described a bifunctional InOOH-O_v electrocatalyst for HMFOR and CO_2 reduction. To gain deeper insights into the structure evolution and reaction process of the electrocatalyst during HMFOR, *in situ* Raman spectra were collected at various potentials. As Fig. 14a shows, two bands at 354 and 459 cm^{-1}, related to In-O, are observable across the entire potential range. The intensity of two bands at 307 and 390 cm^{-1} increases with rising potential, attributable to In-OH stretching vibration modes. This suggests OH ion adsorption and enrichment for the subsequent OER process. For HMFOR, a new peak at 313 cm^{-1}, blue-shifted by 6 cm^{-1} from 307 cm^{-1}, emerges due to competition between HMF molecules and OH^- in the electrolyte (Fig. 14b). More HMF molecules adsorb on the InOOH-O_v surface, initiating HMFOR. However, at potentials over 1.5 V, the peak at 390 cm^{-1} reappears and the one at 313 cm^{-1} shifts back to 307 cm^{-1}, indicating OER's dominance.

Feng *et al.*[21] used *in situ* Raman spectroscopy to examine electrocatalyst structural evolution during MOR. They observed three Raman bands at 468, 533, and 600 cm^{-1} under open circuit potential (OCP), attributed to Ni^{II}–O and Mn^{III}–O. During OER, characteristic bands at 473 and 551 cm^{-1} emerged at 1.37 V *vs.* RHE, indicating Ni^{III}–O in Ni^{III}–OOH (Fig. 14e). These bands were prominent between 1.42–1.52 V *vs.* RHE, suggesting Ni^{III}–OOH stability as the source of OER. In the MOR process, Ni^{III}–O bands also appeared at 1.37 V *vs.* RHE but were less pronounced compared to the original Ni^{II}–O bands within 1.37–1.52 V *vs.* RHE (Fig. 14c). The Ni^{III}–O bands diminished and vanished when the potential decreased from 1.52 to 1.12 V *vs.* RHE. Conversely, the Mn^{III}–O peak at 600 cm^{-1} remained noticeable throughout the potential sweep, indicating Mn ions in NiMn-LDH did not participate in redox transitions, while Ni ions did. Further confirmation of the transition from Ni^{II}–$(OH)_2$ to Ni^{III}–OOH was obtained using *in situ* Raman spectroscopy in deuterium media, showing clearer Ni^{III}–O bands between 1.42–1.52–1.32 V *vs.* RHE (Fig. 14d). This suggests the methanol-induced reduction of Ni^{III}–OOH was impeded due to stronger O–D or C–D bonds with the adsorbate. Similar outcomes were observed with NiFe-LDH as the anode catalyst (Fig. 14f–h). These *in situ* Raman spectroscopy findings indicate the transient and limited formation of Ni^{III}–OOH in NiM-LDHs under optimal MOR conditions, likely as the origin of MOR catalysis.

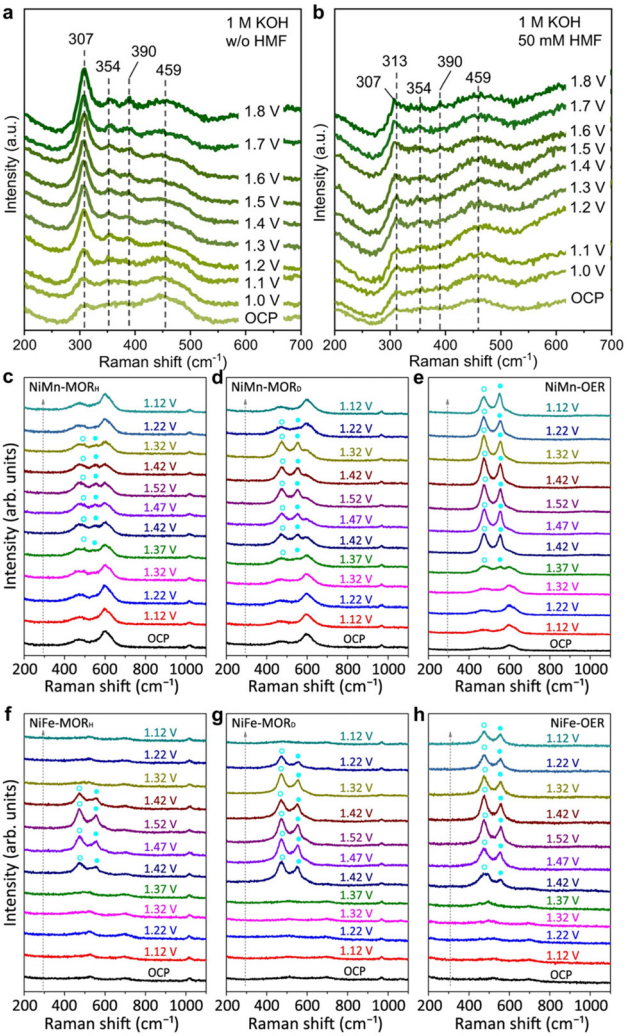

Fig. 14 *In situ* Raman spectra of InOOH-O_v during (a) OER and (b) HMFOR processes. (a and b) Reproduced with permission from ref. 96. Copyright 2023 Springer Nature. Along with the spectra of (c) NiMn and (d) NiFe-LDHs under optimal conditions for MOR (the subscript H or D denotes CH_3OH/H_2O or CD_3OD/D_2O solution) and OER at various potentials. The blue circles highlight the characteristic bands of Ni^{III}–OOH. (c–h) Reproduced with permission from ref. 21. Copyright 2023 Springer Nature.

3.1.3 *In situ* X-ray absorption spectroscopy. *In situ* XAS spectroscopy serves as an effective method for examining changes in target elements during electrochemical reactions, offering crucial insights into the local environment and electronic structure of catalysts. X-ray absorption near edge structure (XANES) is utilized to investigate the dynamic variation in oxidation states or electronic structures of target elements, while extended X-ray absorption fine structures (EXAFS) provide quantitative analysis of changes in local coordination geometry and bond distances.[144]

Duan *et al.*[130] explored the evolution of a high valent Cu mediated region in the electrochemical oxidation of glucose on CuO using *in situ* Cu K edge XANES. The absorption edge energies for CuO–KOH–OCP, CuO–KOH-1.0 V, and CuO–KOH-1.5 V were found between the reference states of Cu_2O and CuO, suggesting a positively charged $Cu^{\delta+}$ state ($1 < \delta < 2$) in these samples (Fig. 15a). This positive charge might originate from oxygen vacancies created during synthesis. Notably, even at a high potential of 1.5 V *vs.* RHE, the valence state of Cu in CuO–KOH-1.5 V was lower than the CuO reference. This is attributed to the formation of CuOOH on CuO's surface, with most of the remaining Cu being defective CuO. These findings, combined with other results, confirmed that the presence of Cu^{3+} species (CuOOH) was due to surface reconstruction in the Cu^{3+} mediated region, not complete reconstruction. Additionally, introducing 0.1 M glucose into the electrolyte decreased the adsorption energy, indicating a reduced valence state of Cu in the samples (Fig. 15b). This reduction was further supported by Cu K edge FT-EXAFS spectra of the Cu^{2+} (Fig. 15c) and Cu^{3+} (Fig. 15d) regions, confirming the reduction of $Cu(OH)_2$ and CuOOH through interaction with glucose. The observed decrease in Cu oxidation state was attributed to the formation of lower-valent Cu species during glucose oxidation, resulting from the reduction of Cu $(OH)_2$ and CuOOH.

These findings underscore the significance of *in situ* XAS spectroscopy in elucidating the dynamic alterations of target elements and their electronic structures during electrochemical reactions, offering valuable insights into catalyst behavior and reaction mechanisms.

3.1.4 Other *in situ* techniques. Wang's group[145] employed *in situ* sum frequency generation (SFG) spectroscopy to elucidate the reaction pathways of HMF electrooxidation over the Ni_3N@C electrocatalyst. Their results indicated that no HMF oxidation occurred at potentials between 1.05 and 1.25 V (Fig. 16a). However, at 1.35 V, HMF oxidation commenced, and the HMF signal diminished. Increasing the potential to 1.45 V revealed features consistent with FFCA or FDCA. At 1.75 V, most characteristic peaks corresponded to FDCA, suggesting FDCA as the final product rather than FFCA. Additionally, *in situ* SFG spectra were recorded at various times under a constant potential of 1.45 V (Fig. 16b), revealing increased prominence of intermediate HMFCA peaks over time. These out-

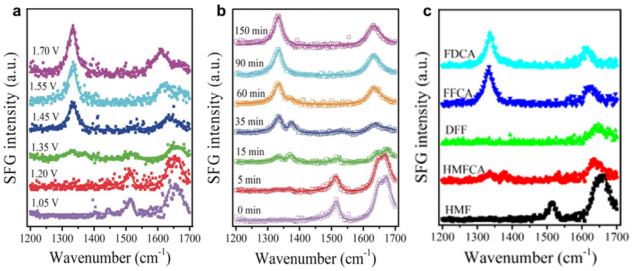

Fig. 16 *In situ* SFG spectra (a) after operating at different potentials for 90 min and (b) at different times during the CA process at a potential of 1.45 V *vs.* RHE. (c) Standard SFG spectra of pure chemicals (FDCA, FFCA, DFF, HMFCA, and HMF). Reproduced with permission from ref. 145. Copyright 2019 Wiley-VCH.

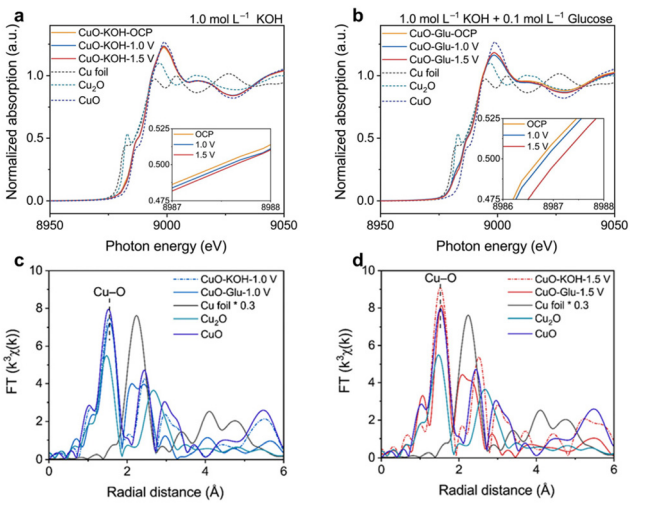

Fig. 15 *In situ* XANES of CuO/CC in electrolytes of (a) 1.0 mol L^{-1} KOH + 10 mmol L^{-1} glucose and (b) 1.0 mol L^{-1} KOH. *In situ* FT-EXAFS spectra of (c) CuO–KOH-1.0 V, CuO–Glu-1.0 V and (d) CuO–KOH-1.5 V, CuO–Glu-1.5 V. Reproduced with permission from ref. 130. Copyright 2023 ELSEVIER.

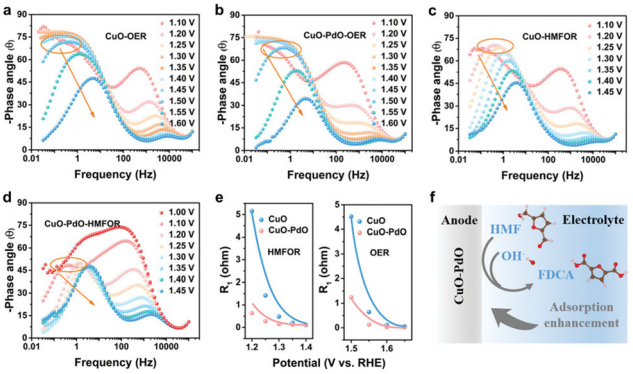

Fig. 17 *In situ* analysis for CuO and CuO–PdO interfaces. (a–d) Bode plots of CuO and CuO–PdO during OER and HMFOR. (e) Fitting R_1 values of CuO and CuO–PdO during OER and HMFOR. (f) Diagram of the initial reaction over CuO–PdO interface in the inner Helmholtz layer. Reproduced with permission from ref.[146] Copyright 2022 Wiley-VCH.

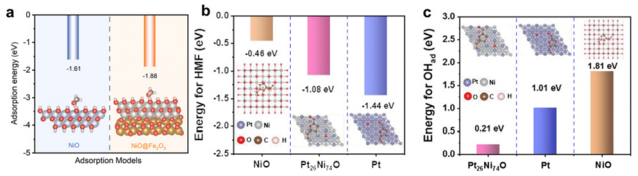

Fig. 18 (a) Calculated absorption energy of methanol on Ni (111) and NiO/Fe_2O_3. (a) Reproduced with permission from ref. 34. Copyright 2023 Royal Society of Chemistry. (b and c) Calculated absorption energy of HMF and OH_{ad} on Pt, NiO, and $Pt_{26}Ni_{74}$ NWs. (b, c) Reproduced with permission from ref. 147. Copyright 2022 American Chemical Society.

comes support the proposed HMFOR reaction pathway *via* path a (Fig. 5), using standard SFG spectra of pure chemicals as references (Fig. 16c).

Zou *et al.*[146] utilized *in situ* electrochemical impedance spectroscopy (EIS) to examine the electrochemical behavior of CuO and CuO–PdO interfaces during HMFOR catalysis. Inflection points (marked by an orange circle) in the low-frequency region of Bode plots at 1.5 V *vs.* RHE indicated OER occurrence at CuO and CuO–PdO interfaces (Fig. 17a and b). CuO exhibited a higher phase angle in the high-frequency region than CuO–PdO, suggesting slower reaction kinetics. During HMFOR, inflection points for CuO and CuO–PdO emerged at lower potentials of 1.2 V and 1.1 V *vs.* RHE, respectively (Fig. 17c and d). This indicated that the CuO–PdO interface required a lower oxidation potential for HMFOR compared to CuO and displayed faster reaction kinetics. CuO–PdO also showed lower charge transfer resistance and a faster reaction rate (Fig. 17e). These analyses conclude that the CuO–PdO interface enhances HMF initial adsorption and accelerates

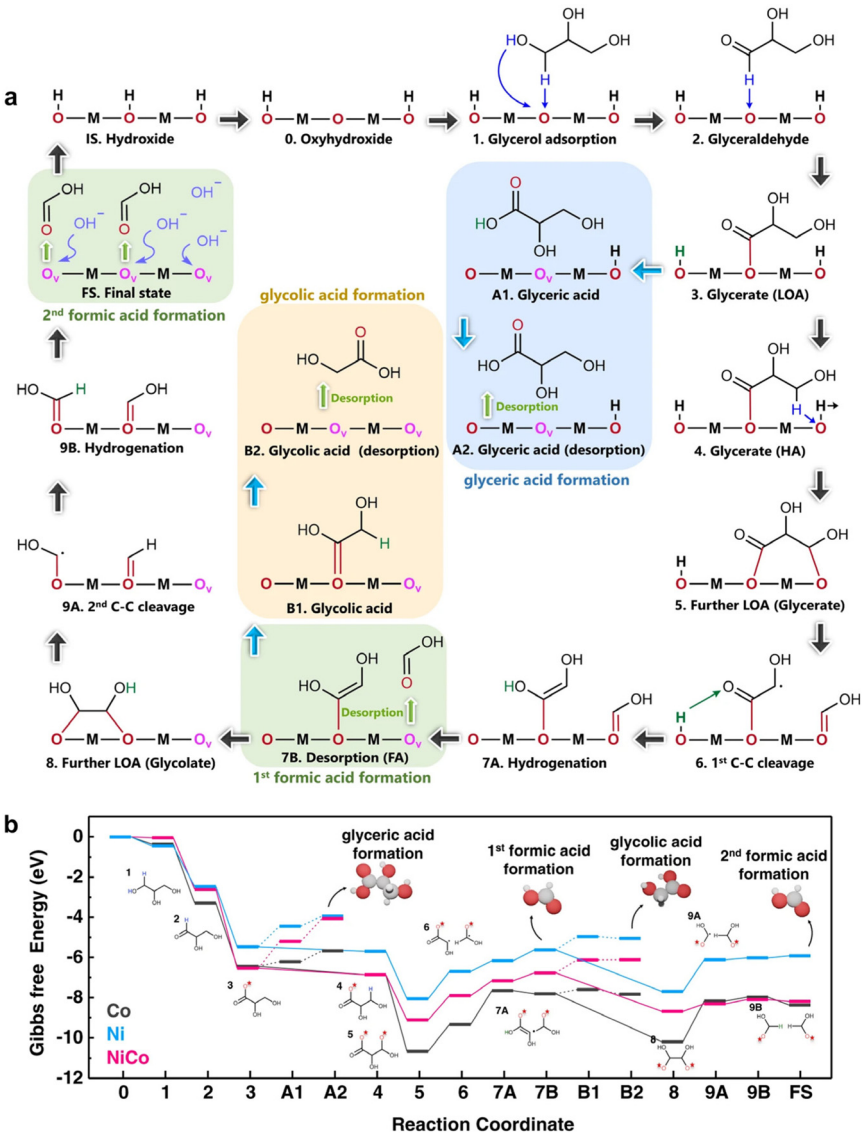

Fig. 19 (a) Schematic illustration of the GOR pathway (b) calculated Gibbs free energy diagrams for GOR on Ni, NiCo, and Co hydroxide. Reproduced with permission from ref. 17. Copyright 2022 Springer Nature.

reaction kinetics (Fig. 17f), exhibiting superior catalytic performance towards HMFOR with increased activity and rate.

3.2 DFT calculations

Understanding the adsorption and desorption behavior of alcohol molecules and OH_{ad} is crucial for designing AOR electrocatalysts.[50] DFT calculations are instrumental in exploring adsorption behavior on electrocatalyst interfaces, providing theoretical insights for electrocatalyst design. Peng *et al.*[34] engineered the NiO/Fe_2O_3 electrocatalyst for MOR, calculating methanol's adsorption energy using DFT (Fig. 18a). Comparisons between the single NiO interface and NiO/Fe_2O_3 interface revealed lower adsorption energy for methanol on NiO/Fe_2O_3, suggesting that electronic interaction between the two metal oxides optimizes alcohol molecule adsorption and improves AOR reaction kinetics. Additionally, Zou and coworkers[147] applied DFT to analyze the synergetic relationship of Pt and Ni in understanding HMF and OH_{ad} adsorption during HMFOR. The calculated adsorption energies of HMF on Pt, $Pt_{26}Ni_{74}$ nanowires (NWs), and NiO indicated strong adsorption on Pt, moderate on $Pt_{26}Ni_{74}$ NWs, and weak on NiO (Fig. 18b). Following the Sabatier principle, $Pt_{26}Ni_{74}$ NWs demonstrated optimal HMF adsorption, as overly strong adsorption can lead to active site poisoning, while weak adsorption may reduce catalytic activity. Moreover, OH_{ad} adsorption energies on these interfaces showed superior OH_{ad} adsorption on $Pt_{26}Ni_{74}$ NWs due to the Pt–O–Ni bond interaction (Fig. 18c). The HMFOR activity is thus enhanced synergistically, with Ni modulating Pt's d-band to alter HMF adsorption, while Pt facilitates OH_{ad} adsorption on Ni. These findings emphasize the importance of DFT calculations in understanding and optimizing molecular adsorption behavior at electrocatalyst interfaces for efficient AOR.

Another vital aspect of DFT calculations is the exploration of the Gibbs free energy of a reaction. Chen *et al.*[17] investigated the electrocatalyst NiCo hydroxide for GOR efficiency. To elucidate the high GOR efficiency in NiCo hydroxide, DFT calculations were performed to unveil the GOR mechanism on Ni, Co, and NiCo hydroxide. Fig. 19a shows the (de)intercalation of protons and oxygen anions in hydroxide as actively involved in elementary reaction steps, including initial electrochemical-driven deintercalation of protons from the electrocatalyst lattice (IS → 0) and deintercalation of oxygen anions during desorption of reaction products (3 → A1 → A2, 7A → 7B, B1 → B2, and 9B → FS). The first dehydrogenation process of adsorbed intermediates (1 → 2, 2 → 3, 4 → 5) was spontaneous, with NiCo hydroxide exhibiting the most negative Gibbs free energy changes compared to Ni and Co hydroxide (Fig. 19b). In the desorption steps (3 → A1 → A2, 7A → 7B, B1 → B2, and 9B → FS), Co hydroxide showed the lowest energy barrier, facilitating product desorption from the catalyst's surface and resulting in diverse products, as confirmed by electrochemical tests. For the 1st C–C bond cleavage steps, similar energy barriers were observed among these catalysts, but NiCo exhibited the lowest energy barrier in the 2nd C–C cleavage step, expediting formic acid formation as GOR's final main product. This aligns with the high efficiency and selectivity of formate production in electrochemical tests from a theoretical perspective.

4. Conclusion and prospect

Recent years have seen considerable interest in the electrochemical conversion of biomass-derived alcohols, driven by the diverse sources of substrates, potential for high-value added products, and milder reaction conditions compared to traditional production methods. In AOR electrocatalysis, advanced non-noble electrocatalysts have been developed and applied across various AOR systems, including monohydric alcohols and polyols oxidation. These non-noble electrocatalysts demonstrate high AOR activity and economic viability compared to noble metal catalysts, which is crucial for transitioning from lab-scale production to practical applications.

Understanding AOR mechanisms is vital for designing efficient electrocatalysts. *in situ* characterization techniques have significantly contributed to this understanding by allowing researchers to observe the structural evolution of electrocatalysts during AOR. This aids in identifying real active sites and reaction intermediates, offering insights for optimizing AOR efficiency. Additionally, theoretical calculations like DFT are employed to study reactant adsorption and desorption properties and determine AOR reaction Gibbs free energy. These calculations guide electrocatalyst design and optimization and aid in screening catalytic materials before experimentation, conserving time and resources. The synergy of advanced electrocatalysts, *in situ* characterization techniques, and theoretical calculations significantly advances the development and optimization of electrochemical methods for biomass-derived alcohol conversion.

While significant progress has been made in the field, several challenges persist: (I) the stability of non-noble metal catalysts for AOR remains inadequate. (II) Relative low selectivity for incomplete oxidation products. (III) Transition metal-based catalysts are mainly focused on the electrooxidation of simple alcohols and lack attention on complex alcohols such as asymmetric alcohols. (IV) Insufficient *in situ* cells can negatively impact test results, affecting the study of reaction mechanisms.

In order to address these challenges, the following aspects should be considered: (I) non-noble metal catalysts offer cost advantages over noble metal electrocatalysts, but their stability for AOR is still lacking. While many studies have focused on enhancing electrocatalyst activity, there has been relatively less emphasis on strategies to improve catalyst stability. Therefore, it is crucial to dedicate more effort to exploring catalyst stability, as it plays a vital role in determining their practical applicability. (II) While most electrocatalysts are typically designed for carboxylic acid product synthesis, there is significant value in incomplete oxidation, which can lead to the production of ketones or aldehydes. It is important to concentrate efforts on adjusting the selectivity of incomplete oxidation products. (III)

The majority of research in this field has concentrated on the electrooxidation of simple alcohols, rather than more complex alcohols like asymmetric alcohols. However, the oxidation products of these complex alcohols, such as chiral compounds, hold great importance in various areas such as drug synthesis, materials production, and other useful applications. Utilizing transition metal-based catalysts for the electrooxidation of asymmetric alcohols can provide a green and sustainable method for producing chiral compounds. (IV) Optimal design of *in situ* reaction cells is crucial for obtaining valuable insights into the reaction process, including tracking intermediates and identifying genuine active sites. Enhancing the design of *in situ* reaction cells is essential to improve signal quality. For example, in certain *in situ* Raman spectroscopic measurements, a thick electrolyte layer between the objective and the target catalyst surface can directly impact signal quality. It is recommended to incorporate an adjustable-height transmission window to reduce the liquid layer thickness or use an immersion lens to enhance signal quality. Additionally, bubbles generated during high potential or high current density conditions from OER can disrupt signal quality, highlighting the importance of researching methods to eliminate these bubbles.

Author contributions

Yuguo Zhao: conceptualization, investigation, visualization, writing – original draft, and writing – review and editing. Emma M. Björk: investigation, supervision and writing – review and editing. Yong Yan: investigation, funding acquisition, supervision and writing – review and editing. Peter Schaaf: supervision and writing – review and editing. Dong Wang: investigation, supervision and writing – review and editing.

Conflicts of interest

There are no conflicts to declare.

Acknowledgements

The present study was funded by the National Natural Science Foundation of China (No. 22278012) and the Swedish Energy Agency (No. 2022-00909).

References

1 S. Chu and A. Majumdar, *Nature*, 2012, **488**, 294–303.
2 P. Prabhu, Y. Wan and J.-M. Lee, *Matter*, 2020, **3**, 1162–1177.
3 A. Kumar, P. Daw and D. Milstein, *Chem. Rev.*, 2022, **122**, 385–441.
4 R. Ge, J. Li and H. Duan, *Sci. China Mater.*, 2022, **65**, 3273–3301.
5 C. Tang, Y. Zheng, M. Jaroniec and S.-Z. Qiao, *Angew. Chem., Int. Ed.*, 2021, **60**, 19572–19590.
6 H. C. Fu, X. H. Chen, B. Yang, Y. H. Luo, T. Li, X. H. Wang, Q. Zhang, X. L. Li, N. B. Li and H. Q. Luo, *Appl. Catal., B*, 2023, **332**, 122739.
7 S. Liu, H. Li, J. Zhong, K. Xu, G. Wu, C. Liu, B. Zhou, Y. Yan, L. Li, W. Cha, K. Chang, Y. Y. Li and J. Lu, Sci. Adv., **8**, eadd6421.
8 Z. Liang, N. Kong, C. Yang, W. Zhang, H. Zheng, H. Lin and R. Cao, *Angew. Chem., Int. Ed.*, 2021, **60**, 12759–12764.
9 Y. Li, F.-M. Li, X.-Y. Meng, S.-N. Li, J.-H. Zeng and Y. Chen, *ACS Catal.*, 2018, **8**, 1913–1920.
10 X. Wang, D. Wu, S. Liu, J. Zhang, X.-Z. Fu and J.-L. Luo, *Nano-Micro Lett.*, 2021, **13**, 125.
11 H. Y. Zhou, Y. B. Qu, J. C. Li, Z. L. Wang, C. C. Yang and Q. Jiang, *Appl. Catal., B*, 2022, **305**, 121023.
12 Y. Song, W. Chen, C. Zhao, S. Li, W. Wei and Y. Sun, *Angew. Chem., Int. Ed.*, 2017, **56**, 10840–10844.
13 T. Dou, J. He, S. Diao, Y. Wang, X. Zhao, F. Zhang and X. Lei, *J. Energy Chem.*, 2023, **82**, 497–506.
14 Y. Qi, Y. Zhang, L. Yang, Y. Zhao, Y. Zhu, H. Jiang and C. Li, *Nat. Commun.*, 2022, **13**, 4602.
15 F. W. S. Lucas, R. G. Grim, S. A. Tacey, C. A. Downes, J. Hasse, A. M. Roman, C. A. Farberow, J. A. Schaidle and A. Holewinski, *ACS Energy Lett.*, 2021, **6**, 1205–1270.
16 G. Bharath and F. Banat, *ACS Appl. Mater. Interfaces*, 2021, **13**, 24643–24653.
17 Z. He, J. Hwang, Z. Gong, M. Zhou, N. Zhang, X. Kang, J. W. Han and Y. Chen, *Nat. Commun.*, 2022, **13**, 3777.
18 M. Yang, Z. Yuan, R. Peng, S. Wang and Y. Zou, *Energy Environ. Mater.*, 2022, **5**, 1117–1138.
19 C.-J. Li and B. M. Trost, *Proc. Natl. Acad. Sci. U. S. A.*, 2008, **105**, 13197–13202.
20 S. Xu, X. Ruan, M. Ganesan, J. Wu, S. K. Ravi and X. Cui, *Adv. Funct. Mater.*, 2024, 2313309.
21 B. Zhu, B. Dong, F. Wang, Q. Yang, Y. He, C. Zhang, P. Jin and L. Feng, *Nat. Commun.*, 2023, **14**, 1686.
22 H. Huang, C. Yu, X. Han, H. Huang, Q. Wei, W. Guo, Z. Wang and J. Qiu, *Energy Environ. Sci.*, 2020, **13**, 4990–4999.
23 Y. Yang and T. Mu, *Green Chem.*, 2021, **23**, 4228–4254.
24 Y. Li, X. Wei, L. Chen, J. Shi and M. He, *Nat. Commun.*, 2019, **10**, 5335.
25 B. You and Y. Sun, *Acc. Chem. Res.*, 2018, **51**, 1571–1580.
26 L. Chen and J. Shi, *J. Mater. Chem. A*, 2018, **6**, 13538–13548.
27 B. Rausch, M. D. Symes and L. Cronin, *J. Am. Chem. Soc.*, 2013, **135**, 13656–13659.
28 H. G. Cha and K.-S. Choi, *Nat. Chem.*, 2015, **7**, 328–333.
29 K.-C. Cheung, W.-L. Wong, D.-L. Ma, T.-S. Lai and K.-Y. Wong, *Coord. Chem. Rev.*, 2007, **251**, 2367–2385.
30 R. Li, K. Xiang, Z. Peng, Y. Zou and S. Wang, *Adv. Energy Mater.*, 2021, **11**, 2102292.
31 H. B. Tao, Y. Xu, X. Huang, J. Chen, L. Pei, J. Zhang, J. G. Chen and B. Liu, *Joule*, 2019, **3**, 1498–1509.

32 S. Xie, Z. Shen, J. Deng, P. Guo, Q. Zhang, H. Zhang, C. Ma, Z. Jiang, J. Cheng, D. Deng and Y. Wang, *Nat. Commun.*, 2018, **9**, 1181.
33 B. Zhao, J. Liu, C. Xu, R. Feng, P. Sui, L. Wang, J. Zhang, J.-L. Luo and X.-Z. Fu, *Adv. Funct. Mater.*, 2021, **31**, 2008812.
34 Y. Hao, D. Yu, S. Zhu, C.-H. Kuo, Y.-M. Chang, L. Wang, H.-Y. Chen, M. Shao and S. Peng, *Energy Environ. Sci.*, 2023, **16**, 1100–1110.
35 X. Peng, S. Xie, X. Wang, C. Pi, Z. Liu, B. Gao, L. Hu, W. Xiao and P. K. Chu, *J. Mater. Chem. A*, 2022, **10**, 20761–20769.
36 K. Zhang, Y. Deng, Y. Wu, L. Wang and L. Yan, *J. Colloid Interface Sci.*, 2023, **647**, 246–254.
37 S. Jiang, T. Xiao, C. Xu, S. Wang, H.-Q. Peng, W. Zhang, B. Liu and Y.-F. Song, *Small*, 2023, **19**, 2208027.
38 S. Bhat, J. Banday and M. Wahid, *Energy Fuels*, 2023, **37**, 6012–6024.
39 K. Zhang, Y. Han, J. Qiu, X. Ding, Y. Deng, Y. Wu, G. Zhang and L. Yan, *J. Colloid Interface Sci.*, 2023, **630**, 570–579.
40 M. Khan, M. I. Abdullah, A. Samad, Z. Shao, T. Mushiana, A. Akhtar, A. Hameed, N. Zhang, U. Schwingenschlögl and M. Ma, *Small*, 2023, **19**, 2205499.
41 D. Wu, W. Zhang and D. Cheng, *ACS Appl. Mater. Interfaces*, 2017, **9**, 19843–19851.
42 H. Wang, L. Cui, S. Yin, H. Yu, K. Deng, Y. Xu, X. Wang, Z. Wang and L. Wang, *J. Mater. Chem. A*, 2022, **10**, 18889–18894.
43 X.-T. Gao, Y.-F. Wang, L. Fu, R.-X. Zhang, R.-M. Li, Z.-H. Gao, Z.-F. Yan, Y.-M. Liu, W. Huang, L. Liu and Z.-J. Zuo, *Int. J. Hydrogen Energy*, 2023, **48**, 32408–32419.
44 J. Wang, B. Zhang, W. Guo, L. Wang, J. Chen, H. Pan and W. Sun, *Adv. Mater.*, 2023, **35**, 2211099.
45 H. Xie, S. Chen, J. Liang, T. Wang, Z. Hou, H.-L. Wang, G. Chai and Q. Li, *Adv. Funct. Mater.*, 2021, **31**, 2100883.
46 F. Galvanin, M. Sankar, S. Cattaneo, D. Bethell, V. Dua, G. J. Hutchings and A. Gavriilidis, *Chem. Eng. J.*, 2018, **342**, 196–210.
47 W. Gao, Y. Song, W. Jiao and Y. Liu, *J. Taiwan Inst. Chem. Eng.*, 2019, **103**, 1–6.
48 J. Li, R. Wei, X. Wang, Y. Zuo, X. Han, J. Arbiol, J. Llorca, Y. Yang, A. Cabot and C. Cui, *Angew. Chem., Int. Ed.*, 2020, **59**, 20826–20830.
49 J. Li, C. Xing, Y. Zhang, T. Zhang, M. C. Spadaro, Q. Wu, Y. Yi, S. He, J. Llorca, J. Arbiol, A. Cabot and C. Cui, *Small*, 2021, **17**, 2006623.
50 W. Chen, C. Xie, Y. Wang, Y. Zou, C.-L. Dong, Y.-C. Huang, Z. Xiao, Z. Wei, S. Du, C. Chen, B. Zhou, J. Ma and S. Wang, *Chem*, 2020, **6**, 2974–2993.
51 W. Wang, Y.-B. Zhu, Q. Wen, Y. Wang, J. Xia, C. Li, M.-W. Chen, Y. Liu, H. Li, H.-A. Wu and T. Zhai, *Adv. Mater.*, 2019, **31**, 1900528.
52 Y. Zhang, W. Zhu, J. Fang, Z. Xu, Y. Xue, D. Liu, R. Sui, Q. Lv, X. Liu, Y. Wang, W. Chen and Z. Zhuang, *Nano Res.*, 2022, **15**, 2987–2993.
53 A. Shekhawat, R. Samanta, S. Panigrahy and S. Barman, *ACS Appl. Energy Mater.*, 2023, **6**, 3135–3146.
54 H. Wang, A. Guan, J. Zhang, Y. Mi, S. Li, T. Yuan, C. Jing, L. Zhang, L. Zhang and G. Zheng, *Chin. J. Catal.*, 2022, **43**, 1478–1484.
55 J. Li, X. Wang, C. Xing, L. Li, S. Mu, X. Han, R. He, Z. Liang, P. Martinez, Y. Yi, Q. Wu, H. Pan, J. Arbiol, C. Cui, Y. Zhang and A. Cabot, *Chem. Eng. J.*, 2022, **440**, 135817.
56 J. Wan, X. Mu, Y. Jin, J. Zhu, Y. Xiong, T. Li and R. Li, *Green Chem.*, 2022, **24**, 4870–4876.
57 X. Chen, X. Zhong, B. Yuan, S. Li, Y. Gu, Q. Zhang, G. Zhuang, X. Li, S. Deng and J.-g. Wang, *Green Chem.*, 2019, **21**, 578–588.
58 R. Li, P. Kuang, L. Wang, H. Tang and J. Yu, *Chem. Eng. J.*, 2022, **431**, 134137.
59 L. Ming, X.-Y. Wu, S.-S. Wang, W. Wu and C.-Z. Lu, *Green Chem.*, 2021, **23**, 7825–7830.
60 B. You, X. Liu, X. Liu and Y. Sun, *ACS Catal.*, 2017, **7**, 4564–4570.
61 X. Song, X. Liu, H. Wang, Y. Guo and Y. Wang, *Ind. Eng. Chem. Res.*, 2020, **59**, 17348–17356.
62 H. Wang, C. Li, J. An, Y. Zhuang and S. Tao, *J. Mater. Chem. A*, 2021, **9**, 18421–18430.
63 W.-J. Liu, L. Dang, Z. Xu, H.-Q. Yu, S. Jin and G. W. Huber, *ACS Catal.*, 2018, **8**, 5533–5541.
64 B. Zhang, H. Fu and T. Mu, *Green Chem.*, 2022, **24**, 877–884.
65 P. Zhang, X. Sheng, X. Chen, Z. Fang, J. Jiang, M. Wang, F. Li, L. Fan, Y. Ren, B. Zhang, B. J. J. Timmer, M. S. G. Ahlquist and L. Sun, *Angew. Chem., Int. Ed.*, 2019, **58**, 9155–9159.
66 L. Gao, Z. Liu, J. Ma, L. Zhong, Z. Song, J. Xu, S. Gan, D. Han and L. Niu, *Appl. Catal., B*, 2020, **261**, 118235.
67 M. J. Kang, H. Park, J. Jegal, S. Y. Hwang, Y. S. Kang and H. G. Cha, *Appl. Catal., B*, 2019, **242**, 85–91.
68 G. Yang, Y. Jiao, H. Yan, Y. Xie, A. Wu, X. Dong, D. Guo, C. Tian and H. Fu, *Adv. Mater.*, 2020, **32**, 2000455.
69 R. Ge, Y. Wang, Z. Li, M. Xu, S.-M. Xu, H. Zhou, K. Ji, F. Chen, J. Zhou and H. Duan, *Angew. Chem., Int. Ed.*, 2022, **61**, e202200211.
70 L. Zeng, Y. Chen, M. Sun, Q. Huang, K. Sun, J. Ma, J. Li, H. Tan, M. Li, Y. Pan, Y. Liu, M. Luo, B. Huang and S. Guo, *J. Am. Chem. Soc.*, 2023, **145**, 17577–17587.
71 W. Jia, B. Liu, R. Gong, X. Bian, S. Du, S. Ma, Z. Song, Z. Ren and Z. Chen, *Small*, 2023, **19**, 2302025.
72 Y. Song, W. Xie, Y. Song, H. Li, S. Li, S. Jiang, J. Y. Lee and M. Shao, *Appl. Catal., B*, 2022, **312**, 121400.
73 H. Zhou, Y. Ren, Z. Li, M. Xu, Y. Wang, R. Ge, X. Kong, L. Zheng and H. Duan, *Nat. Commun.*, 2021, **12**, 4679.
74 F. Liu, X. Gao, R. Shi, Z. Guo, E. C. M. Tse and Y. Chen, *Angew. Chem., Int. Ed.*, 2023, **62**, e202300094.
75 J. Li, L. Li, X. Ma, X. Han, C. Xing, X. Qi, R. He, J. Arbiol, H. Pan, J. Zhao, J. Deng, Y. Zhang, Y. Yang and A. Cabot, *Adv. Sci.*, 2023, **10**, 2300841.
76 Y. Xu, M. Liu, S. Wang, K. Ren, M. Wang, Z. Wang, X. Li, L. Wang and H. Wang, *Appl. Catal., B*, 2021, **298**, 120493.

77 L. Dong, G.-R. Chang, Y. Feng, X.-Z. Yao and X.-Y. Yu, *Rare Met.*, 2022, **41**, 1583–1594.
78 X. Yu, R. B. Araujo, Z. Qiu, E. Campos dos Santos, A. Anil, A. Cornell, L. G. M. Pettersson and M. Johnsson, *Adv. Energy Mater.*, 2022, **12**, 2103750.
79 Y. Wang, Y.-Q. Zhu, Z. Xie, S.-M. Xu, M. Xu, Z. Li, L. Ma, R. Ge, H. Zhou, Z. Li, X. Kong, L. Zheng, J. Zhou and H. Duan, *ACS Catal.*, 2022, **12**, 12432–12443.
80 L. Fan, Y. Ji, G. Wang, Z. Zhang, L. Yi, K. Chen, X. Liu and Z. Wen, *J. Energy Chem.*, 2022, **72**, 424–431.
81 Y. Li, X. Wei, S. Han, L. Chen and J. Shi, *Angew. Chem., Int. Ed.*, 2021, **60**, 21464–21472.
82 Q. Qian, X. He, Z. Li, Y. Chen, Y. Feng, M. Cheng, H. Zhang, W. Wang, C. Xiao, G. Zhang and Y. Xie, *Adv. Mater.*, 2023, **35**, 2300935.
83 W.-J. Liu, Z. Xu, D. Zhao, X.-Q. Pan, H.-C. Li, X. Hu, Z.-Y. Fan, W.-K. Wang, G.-H. Zhao, S. Jin, G. W. Huber and H.-Q. Yu, *Nat. Commun.*, 2020, **11**, 265.
84 D. Li, Y. Huang, Z. Li, L. Zhong, C. Liu and X. Peng, *Chem. Eng. J.*, 2022, **430**, 132783.
85 Y. Zhang, B. Zhou, Z. Wei, W. Zhou, D. Wang, J. Tian, T. Wang, S. Zhao, J. Liu, L. Tao and S. Wang, *Adv. Mater.*, 2021, **33**, 2104791.
86 J. Zheng, X. Chen, X. Zhong, S. Li, T. Liu, G. Zhuang, X. Li, S. Deng, D. Mei and J.-G. Wang, *Adv. Funct. Mater.*, 2017, **27**, 1704169.
87 G. Han, Y.-H. Jin, R. A. Burgess, N. E. Dickenson, X.-M. Cao and Y. Sun, *J. Am. Chem. Soc.*, 2017, **139**, 15584–15587.
88 Y. Gao, L. Ge, H. Xu, K. Davey, Y. Zheng and S.-Z. Qiao, *ACS Catal.*, 2023, **13**, 11204–11231.
89 G. Zhao, G. Hai, P. Zhou, Z. Liu, Y. Zhang, B. Peng, W. Xia, X. Huang and G. Wang, *Adv. Funct. Mater.*, 2023, **33**, 2213170.
90 G. Chen, X. Li and X. Feng, *Angew. Chem., Int. Ed.*, 2022, **61**, e202209014.
91 C. Chen, Z. Zhou, J. Liu, B. Zhu, H. Hu, Y. Yang, G. Chen, M. Gao and J. Zhang, *Appl. Catal., B*, 2022, **307**, 121209.
92 H. Zhou, Y. Ren, B. Yao, Z. Li, M. Xu, L. Ma, X. Kong, L. Zheng, M. Shao and H. Duan, *Nat. Commun.*, 2023, **14**, 5621.
93 R. Zhong, P. Wu, Q. Wang, X. Zhang, L. Du, Y. Liu, H. Yang, M. Gu, Z. C. Zhang, L. Huang and S. Ye, *Green Chem.*, 2023, **25**, 4674–4684.
94 K. A. P. Payne, S. A. Marshall, K. Fisher, M. J. Cliff, D. M. Cannas, C. Yan, D. J. Heyes, D. A. Parker, I. Larrosa and D. Leys, *ACS Catal.*, 2019, **9**, 2854–2865.
95 D. Xiao, X. Bao, D. Dai, Y. Gao, S. Si, Z. Wang, Y. Liu, P. Wang, Z. Zheng, H. Cheng, Y. Dai and B. Huang, *Adv. Mater.*, 2023, **35**, 2304133.
96 F. Ye, S. Zhang, Q. Cheng, Y. Long, D. Liu, R. Paul, Y. Fang, Y. Su, L. Qu, L. Dai and C. Hu, *Nat. Commun.*, 2023, **14**, 2040.
97 S. Fan, B. Zhu, Y. Zhong, S. Shi, J. Zhang and C. Chen, *Chem. Eng. J.*, 2023, **474**, 145905.
98 D. J. Chadderdon, L. Xin, J. Qi, Y. Qiu, P. Krishna, K. L. More and W. Li, *Green Chem.*, 2014, **16**, 3778–3786.
99 D. Bonincontro, A. Lolli, A. Villa, L. Prati, N. Dimitratos, G. M. Veith, L. E. Chinchilla, G. A. Botton, F. Cavani and S. Albonetti, *Green Chem.*, 2019, **21**, 4090–4099.
100 S. Fan, B. Zhu, X. Yu, Y. Gao, W. Xie, Y. Yang, J. Zhang and C. Chen, *J. Energy Chem.*, 2024, **92**, 1–7.
101 D. Chen, Y. Ding, X. Cao, L. Wang, H. Lee, G. Lin, W. Li, G. Ding and L. Sun, *Angew. Chem., Int. Ed.*, 2023, **62**, e202309478.
102 S. Li, S. Wang, Y. Wang, J. He, K. Li, Y. Xu, M. Wang, S. Zhao, X. Li, X. Zhong and J. Wang, *Adv. Funct. Mater.*, 2023, **33**, 2214488.
103 Y. Sun, J. Wang, Y. Qi, W. Li and C. Wang, *Adv. Sci.*, 2022, **9**, 2200957.
104 C. Liu, X.-R. Shi, K. Yue, P. Wang, K. Zhan, X. Wang, B. Y. Xia and Y. Yan, *Adv. Mater.*, 2023, **35**, 2211177.
105 R. Zhang, F. Gao, C. Yang, Y. Bian, G. Wang, K. Xue, J. Zhang, C. Wang and X. Gao, *Mater. Today Nano*, 2023, **23**, 100373.
106 J. Wu, Z. Zhai, T. Yu, X. Wu, S. Huang, W. Cao, Y. Jiang, J. Pei and S. Yin, *J. Energy Chem.*, 2023, **86**, 480–489.
107 Z. Li, L. Huai, P. Hao, X. Zhao, Y. Wang, B. Zhang, C. Chen and J. Zhang, *Chin. J. Catal.*, 2022, **43**, 793–801.
108 B. Zhu, C. Chen, L. Huai, Z. Zhou, L. Wang and J. Zhang, *Appl. Catal., B*, 2021, **297**, 120396.
109 J. Liu, B. Zhu, Y. Zhong, S. Fan, L. Huai, H. Hu, Y. Yang, J. Zhang and C. Chen, *Chem. Eng. J.*, 2023, **472**, 144877.
110 W. Luo, H. Tian, Q. Li, G. Meng, Z. Chang, C. Chen, R. Shen, X. Yu, L. Zhu, F. Kong, X. Cui and J. Shi, *Adv. Funct. Mater.*, 2024, **34**, 2306995.
111 D. Liu, J. C. Liu, W. Cai, J. Ma, H. B. Yang, H. Xiao, J. Li, Y. Xiong, Y. Huang and B. Liu, *Nat. Commun.*, 2019, **10**, 1779.
112 Z. He, X. Ning, G. Yang, H. Wang, Y. Cao, F. Peng and H. Yu, *Catal. Today*, 2021, **365**, 162–171.
113 S. Bagheri, N. M. Julkapli and W. A. Yehye, *Renewable Sustainable Energy Rev.*, 2015, **41**, 113–127.
114 A. Behr, J. Eilting, K. Irawadi, J. Leschinski and F. Lindner, *Green Chem.*, 2008, **10**, 13–30.
115 Y. Li and F. Zaera, *J. Catal.*, 2015, **326**, 116–126.
116 H. Yan, S. Yao, W. Liang, S. Zhao, X. Jin, X. Feng, Y. Liu, X. Chen and C. Yang, *J. Catal.*, 2020, **381**, 248–260.
117 T. Zhan, W. Liu, J. Teng, C. Yue, D. Li, S. Wang and H. Tan, *Chem. Commun.*, 2019, **55**, 2620–2623.
118 J. Cai, H. Ma, J. Zhang, Z. Du, Y. Huang, J. Gao and J. Xu, *Chin. J. Catal.*, 2014, **35**, 1653–1660.
119 L. Xin, Z. Zhang, Z. Wang and W. Li, *ChemCatChem*, 2012, **4**, 1105–1114.
120 M. Sankar, N. Dimitratos, D. W. Knight, A. F. Carley, R. Tiruvalam, C. J. Kiely, D. Thomas and G. J. Hutchings, *ChemSusChem*, 2009, **2**, 1145–1151.
121 Y. Zhan, W. Hou, G. Li, Y. Shen, Y. Zhang and Y. Tang, *ACS Sustainable Chem. Eng.*, 2019, **7**, 17559–17564.
122 K. Kong, D. Li, W. Ma, Q. Zhou, G. Tang and Z. Hou, *Chin. J. Catal.*, 2019, **40**, 534–542.

123 Y. Xiong, J. Dong, Z. Q. Huang, P. Xin, W. Chen, Y. Wang, Z. Li, Z. Jin, W. Xing, Z. Zhuang, J. Ye, X. Wei, R. Cao, L. Gu, S. Sun, L. Zhuang, X. Chen, H. Yang, C. Chen, Q. Peng, C. R. Chang, D. Wang and Y. Li, *Nat. Nanotechnol.*, 2020, **15**, 390–397.
124 Y.-B. Huang and Y. Fu, *Green Chem.*, 2013, **15**, 1095–1111.
125 M. Grasemann and G. Laurenczy, *Energy Environ. Sci.*, 2012, **5**, 8171–8181.
126 W. Deng, Q. Zhang and Y. Wang, *Catal. Today*, 2014, **234**, 31–41.
127 P. Pal, R. Kumar and S. Banerjee, *Chem. Eng. Process.*, 2016, **104**, 160–171.
128 T. N. Smith, K. Hash, C.-L. Davey, H. Mills, H. Williams and D. E. Kiely, *Carbohydr. Res.*, 2012, **350**, 6–13.
129 Y.-Q. Zhu, H. Zhou, J. Dong, S.-M. Xu, M. Xu, L. Zheng, Q. Xu, L. Ma, Z. Li, M. Shao and H. Duan, *Angew. Chem., Int. Ed.*, 2023, **62**, e202219048.
130 Y. Wang, M. Xu, X. Wang, R. Ge, Y.-Q. Zhu, A.-Z. Li, H. Zhou, F. Chen, L. Zheng and H. Duan, *Sci. Bull.*, 2023, **68**, 2982–2992.
131 D. Zheng, J. Li, S. Ci, P. Cai, Y. Ding, M. Zhang and Z. Wen, *Appl. Catal., B*, 2020, **277**, 119178.
132 L. Ostervold, S. I. Perez Bakovic, J. Hestekin and L. F. Greenlee, *RSC Adv.*, 2021, **11**, 31208–31218.
133 M. P. J. M. van der Ham, E. van Keulen, M. T. M. Koper, A. A. Tashvigh and J. H. Bitter, *Angew. Chem., Int. Ed.*, 2023, **62**, e202306701.
134 Z. Song, T. Shen, Y. Hu, G. Liu, S. Bai, X. Sun, S.-M. Xu and Y.-F. Song, *Nanoscale*, 2023, **15**, 11867–11874.
135 Z. Li, Y. Yan, S.-M. Xu, H. Zhou, M. Xu, L. Ma, M. Shao, X. Kong, B. Wang, L. Zheng and H. Duan, *Nat. Commun.*, 2022, **13**, 147.
136 J.-T. Li, Z.-Y. Zhou, I. Broadwell and S.-G. Sun, *Acc. Chem. Res.*, 2012, **45**, 485–494.
137 Y. He, S. Liu, M. Wang, Q. Cheng, H. Ji, T. Qian and C. Yan, *Energy Environ. Mater.*, 2022, **6**, e12552.
138 C. Lamberti, A. Zecchina, E. Groppo and S. Bordiga, *Chem. Soc. Rev.*, 2010, **39**, 4951–5001.
139 R. Mendelsohn, G. Mao and C. R. Flach, *Biochim. Biophys. Acta, Biomembr.*, 2010, **1798**, 788–800.
140 T. Petit and L. Puskar, *Diamond Relat. Mater.*, 2018, **89**, 52–66.
141 S. Li, R. Ma, J. Hu, Z. Li, L. Liu, X. Wang, Y. Lu, G. E. Sterbinsky, S. Liu, L. Zheng, J. Liu, D. Liu and J. Wang, *Nat. Commun.*, 2022, **13**, 2916.
142 K. Shi, D. Si, X. Teng, L. Chen and J. Shi, *Chin. J. Catal.*, 2023, **53**, 143–152.
143 H.-Q. Chen, L. Zou, D.-Y. Wei, L.-L. Zheng, Y.-F. Wu, H. Zhang and J.-F. Li, *Chin. J. Catal.*, 2022, **43**, 33–46.
144 T. Zhao, Y. Wang, S. Karuturi, K. Catchpole, Q. Zhang and C. Zhao, *Carbon Energy*, 2020, **2**, 582–613.
145 N. Zhang, Y. Zou, L. Tao, W. Chen, L. Zhou, Z. Liu, B. Zhou, G. Huang, H. Lin and S. Wang, *Angew. Chem., Int. Ed.*, 2019, **58**, 15895–15903.
146 P. Zhou, X. Lv, S. Tao, J. Wu, H. Wang, X. Wei, T. Wang, B. Zhou, Y. Lu, T. Frauenheim, X. Fu, S. Wang and Y. Zou, *Adv. Mater.*, 2022, **34**, 2204089.
147 J. Wu, Z. Kong, Y. Li, Y. Lu, P. Zhou, H. Wang, L. Xu, S. Wang and Y. Zou, *ACS Nano*, 2022, **16**, 21518–21526.